The LC3B FRET biosensor monitors the modes of action of ATG4B during autophagy in living cells

Elif Begüm Gökerküçük[1], Angélique Chéron[1], Marc Tramier[1,*], Giulia Bertolin[1,2,*].

[1] Univ Rennes, CNRS, IGDR (Institute of Genetics and Development of Rennes), UMR 6290, F-35000 Rennes, France

[2] Lead contact

[*] Correspondence and requests for materials should be addressed to G.B. (giulia.bertolin@univ-rennes1.fr; Tel: +330223237516) or to M.T. (marc.tramier@univ-rennes1.fr; Tel: +330223235487).

Abstract

Although several mechanisms of autophagy have been dissected in the last decade, following this pathway in real time remains challenging. Among the early events leading to its activation, the ATG4B protease primes the key autophagy player LC3B. Given the lack of reporters to follow this event in living cells, we developed a Förster's Resonance Energy Transfer (FRET) biosensor responding to the priming of LC3B by ATG4B. The biosensor was generated by flanking LC3B within a pH-resistant donor-acceptor FRET pair, Aquamarine/tdLanYFP. We here showed that the biosensor has a dual readout. First, FRET indicates the priming of LC3B by ATG4B and the resolution of the FRET image allows to characterize the spatial heterogeneity of the priming activity. Second, quantifying the number of Aquamarine-LC3B puncta determines the degree of autophagy activation. We then showed that there are pools of unprimed LC3B upon *ATG4B* downregulation, and that the priming of the biosensor is abolished in *ATG4B* knockout cells. The lack of priming can be rescued with the wild-type ATG4B or with the partially active W142A mutant, but not with the catalytically dead C74S mutant. Moreover, we screened for commercially-available ATG4B inhibitors, and we illustrated their differential mode of action by implementing a spatially-resolved, broad-to-sensitive analysis pipeline combining FRET and the quantification of autophagic puncta. Finally, we uncovered the CDK1-dependent regulation of the ATG4B-LC3B axis at mitosis. Therefore, the LC3B FRET biosensor paves the way for a highly-quantitative monitoring of

32   the ATG4B activity in living cells and in real time, with unprecedented spatiotemporal

33   resolution.

34

35   Keywords: ATG4B; autophagy; biosensor; FRET/FLIM; LC3B

36   Abbreviations: ATG: autophagy-related; AURKA: Aurora kinase A; BafA$_1$: Bafilomycin A$_1$;

37   CDK1: Cyclin-dependent kinase 1; DKO: double knockout; FLIM: fluorescence lifetime

38   imaging microscopy; FRET: Förster's resonance energy transfer; GABARAP: gamma-

39   aminobutyric acid (GABA) type A receptor-associated protein; HBSS: Hank's balanced salt

40   solution; KO: knockout; LAMP2: lysosomal associated membrane protein 2; MAP1LC3/LC3:

41   microtubule-associated protein 1 light chain 3; mTORC1: mammalian target of rapamycin

42   complex 1; NSC: NSC 185058; PE: phosphatidylethanolamine; SKO: single knockout; TFEB:

43   Transcription Factor EB; TKO: triple knockout; ULK1: Unc-51 like autophagy activating

44   kinase 1; ZPCK: *Z-L*-phe chloromethyl ketone

Introduction

46   Conserved in all eukaryotic cells, macroautophagy/autophagy is the lysosome-mediated degradation and

47   recycling of the intracellular components [1]. Autophagy is triggered as a survival response in paradigms such

48   as starvation, pathogen infection or DNA damage, and it contributes to cellular differentiation, immunity,

49   aging and cell death [2–4]. In mammals, autophagy starts at sites of endoplasmic reticulum (ER) enriched for

50   phosphatidylinositol 3-phosphate [PI(3)P]. On these subdomains, a double-membrane structure termed

51   phagophore forms [5]. As the phagophore elongates into a crescent-shaped structure, it engulfs bulk or

52   selective cargoes and then closes into a double-membrane vesicle, the autophagosome. The fusion of

53   autophagosomes with lysosomes results in the degradation of the sequestered cargo by the lysosomal acid

54   hydrolases.

A series of AuTophaGy-related (ATG) proteins regulate the autophagic pathway [6]. Among them, a special attention is given to the ATG8 family, which are the key proteins found on autophagosomal membranes at all stages of the pathway. ATG8 proteins are ubiquitin-like adaptor proteins involved in autophagosome formation, biogenesis and cargo selection [7–9]. In mammals, ATG8 proteins belong to two subfamilies, the MAP1LC3/LC3 (microtubule-associated protein 1 light chain 3) and GABARAP (gamma-aminobutyric acid [GABA] type A receptor-associated protein) [10,11]. A total of seven genes - *LC3A*, *LC3B*, *LC3B2*, *LC3C*, *GABARAP*, *GABARAPL1* and *GABARAPL2* - code for the LC3 and GABARAP subfamilies in humans [10]. LC3/GABARAPs are found as inactive pro- forms upon translation, and are activated by the ATG4 family of cysteine proteases [12,13]. In humans, four members of the ATG4 family (ATG4A, B, C and D) are responsible for this activation step, which is to proteolytically cleave the C-terminus of pro-LC3/GABARAP proteins and convert them into the so-called form-I. This crucial cleavage is known as "pro-LC3/GABARAP priming", and it is essential to expose a specific glycine residue required for the lipidation of the cytosolic LC3/GABARAP-I proteins to the phosphatidylethanolamine (PE) head groups of the forming phagophores. This is achieved after a series of reactions that involves the E1-like enzyme ATG7, the E2-like enzyme ATG3 and the E3-like complex ATG12–ATG5-ATG16L1 [12,14–16]. The PE-conjugated LC3/GABARAP proteins are then called LC3/GABARAP-II, and function in membrane tethering, hemifusion, autophagosome formation and cargo recruitment [17–20]. Once the phagophore is fully closed, LC3/GABARAP-II proteins are removed from the outer surface of the phagophore membrane by ATG4s, through the hydrolysis of the link between PE and LC3/GABARAP [12]. Although the importance of this second round of cleavage activity (referred as deconjugation hereafter) by ATG4 was shown to be important for the normal progression of autophagy in yeast [21–23], recent studies in human cells suggest the existence of autophagy-independent roles for the deconjugation activity of ATG4s [24,25]. Therefore, the relevance of ATG4-mediated deconjugation for the progression and completion of autophagy in models other than yeast still requires further investigation [21–26].

79   Autophagy plays an essential role to maintain cellular homeostasis, and its dysfunction has been

80   implicated in many pathological conditions such as neurodegenerative diseases, cancer, inflammation,

81   muscular and hearth disorders [27]. As a consequence, therapeutic options to modulate autophagy emerged as

82   promising strategies for the treatment of these complex pathologies [28]. In this light, targeting ATG4s to

83   inhibit autophagy in its early stages has a significant potential to completely block autophagy [29]. However,

84   currently available compounds targeting ATG4 activity show poor specificity and/or efficacy [30]. In addition,

85   there is a lack of dedicated probes that can be used in living cells to monitor ATG4 activity during autophagy

86   progression. Overall, this creates a bottleneck for the identification of ATG4 inhibitors with improved

87   properties. For these reasons, we developed a Förster's Resonance Energy Transfer (FRET) biosensor, named

88   the LC3B biosensor, to simultaneously monitor: 1) the priming of LC3B by ATG4 and 2) the accumulation

89   of LC3B on the autophagic membranes.

90   The FRET phenomenon is a non-radiative energy transfer between a donor and an acceptor pair of

91   fluorophores. FRET can occur when the emission spectrum of the donor fluorophore partially overlaps with

92   the excitation spectrum of the acceptor, and this only when the two fluorescent moieties are in close proximity

93   (less than 10 nm apart) [31]. This phenomenon can be used to monitor many different cellular events including

94   the exploration of protein-protein interactions, the changes in conformation of proteins, and the up- or

95   downregulation of signaling pathways [32,33]. With the recent advances, FRET quantification by fluorescence

96   lifetime imaging microscopy (FLIM) became a very useful method to study molecular activities in living cells

97   [34].

98   In this study, we present the LC3B biosensor as a superior probe that can be used in living cells to

99   monitor the activation – LC3B priming by ATG4 – and progression – LC3B accumulation on the autophagic

100   membranes – of autophagy, in real time and with high spatial resolution. We show that the biosensor

101   recapitulates the main features of the endogenous LC3B protein in terms of forming puncta-shaped structures,

102   of ATG4B-dependent cleavage, and of its colocalization with lysosomal proteins upon autophagy induction

103   and/or lysosomal inhibition. We also show that the biosensor can report on the changes in proLC3B priming,

104 and this in an ATG4B-dependent manner. Using *ATG4* knockout cells, we demonstrate that the absence of

105 ATG4B maximizes the FRET response of the biosensor as a consequence of the complete lack of proLC3B

106 priming. We then show that proLC3B priming can be rescued with the ectopic expression of the wild-type

107 ATG4B. Interestingly, we demonstrate that the ATG4B^{W142A} mutant, previously shown to possess a

108 significantly reduced catalytic activity [35], is capable of rescuing proLC3B priming similarly to the wild-

109 type protein. By using the LC3B biosensor and performing multiple approaches to analyze FRET/FLIM, we

110 report on the action of mechanisms of available ATG4 inhibitors. By doing so, we provide a framework of

111 how to use the LC3B biosensor and analyze the acquired data to identify new ATG4 inhibitors with better

112 specificity and efficacy. Finally, we used the biosensor to reveal the involvement of the cell cycle protein

113 CDK1 in the ATG4B-LC3B axis at mitosis, a cell cycle phase where the involvement of autophagy is still

114 controversial.

115 **Results**

116 *The LC3B biosensor dynamically reports on the activation or the inhibition of the autophagy flux, and it*

117 *colocalizes with LAMP2 in an autophagy-dependent manner*

118 To monitor the priming activity of ATG4 in real time and with spatial resolution, we developed a FRET-based

119 biosensor that can be utilized in living cells. We chose LC3B as it is a known target of the ATG4 activity that

120 undergoes an ATG4-mediated cleavage on Gly120, and it is among the best characterized players of the

121 autophagy pathway [36]. The biosensor was designed to flank the N- and C-termini of proLC3B with a donor-

122 acceptor FRET pair (Fig. 1A). The FRET pair composed of Aquamarine (donor, cyan) and tdLanYFP

123 (acceptor, yellow) was selected on the resistance of both fluorophores to acidic pH [37–39]. In the absence of

124 ATG4 activity, the LC3B biosensor is expected to remain unprocessed in cells, allowing Aquamarine and

125 tdLanYFP to perform FRET (Fig. 1A). If ATG4 is active, the biosensor is expected to undergo an ATG4-

126 dependent proteolytic cleavage at its C-terminus, thereby losing the tdLanYFP moiety and the FRET effect

127 with it. This allows to follow the initial C-terminal priming activity of ATG4 as an early, FRET-based readout.

128 In addition, the priming of LC3B leads to its conversion into the I form, which will still be tagged by

129 Aquamarine (Aquamarine-LC3B-I). When the resulting Aquamarine-LC3B-I protein is integrated into the PE

130 head groups of the phagophores, the biosensor is expected to function as a canonical fluorescent probe to

131 quantify LC3B-positive puncta structures. Therefore, our biosensor also provides a quantitative readout on

132 the late stages of the autophagic pathway, and it can be used to estimate the number of autophagosomes in

133 individual cells (Fig. 1A).

134 We first explored whether the LC3B biosensor is capable of localizing to autophagosomes, which

135 normally appear as puncta-shaped structures. In U2OS cells transiently transfected to express the biosensor,

136 Aquamarine was observed to be present both in puncta-shaped structures, which are compatible with LC3B-

137 II, and in the cytosol, which is compatible with Aqua-LC3B-I (Fig. 1B). To confirm that the puncta-shaped

138 structures were autophagosomes, cells were treated with autophagy inducers as Torin1 or HBSS, in the

139 presence or absence of the lysosomal inhibitor Bafilomycin A$_1$ (BafA$_1$). Compared to control cells, a

140 significant increase in the number of Aquamarine-positive puncta was observed in cells expressing the wild-

141 type LC3B biosensor (WT biosensor) and treated with BafA$_1$ or Torin1 alone (Fig. 1B, C). A further increase

142 in the number of Aquamarine-positive puncta was observed when cells were treated simultaneously with

143 BafA$_1$ and Torin1. This indicates that the puncta-shaped structures observed under these conditions are

144 Aquamarine-LC3B-II (Aqua-LC3B-II)-positive autophagosomes, since they respond to autophagy induction

145 and to lysosomal inhibition alone or in combination. Conversely, autophagy induction by starvation did not

146 cause any increase in the number of puncta-shaped structures when compared to the control (Fig. 1B, C).

147 However, when starvation with HBSS was coupled with BafA$_1$ treatment, we observed a significant

148 accumulation of puncta-shaped structures (Fig. 1B, C). In all conditions tested, tdLanYFP appeared to be

149 diffused in the cytosol, thereby showing a dramatic difference compared to the distribution of Aquamarine

150 into puncta-shaped structures. This strongly suggests that tdLanYFP is cleaved along with the C-terminal part

151 of proLC3B, and therefore it cannot colocalize with Aquamarine on the puncta-shaped structures. To

152 corroborate this observation, we explored the distribution of an uncleavable variant of the LC3B biosensor,

153   which is mutated on Gly120 (hereby, G120A biosensor) and cannot be primed by ATG4 [36]. In cells

154   expressing the G120A biosensor, both Aquamarine and tdLanYFP were exclusively diffused in the cytosol

155   (Fig. S1), and they exhibited no puncta-shaped structures under any treatment (Fig. 1C and S1). The difference

156   in puncta numbers between the WT and the G120A biosensors supports the notion that the WT construct is

157   cleaved at the C-ter, and that it efficiently forms autophagosome-related puncta structures. In this light, we

158   verified the cleavage profiles of the WT and G120A biosensors by western blotting. While the G120A

159   biosensor had a molecular weight of ~95 kDa – corresponding to Aquamarine + proLC3B^{G120A} + tdLanYFP

160   –, the WT biosensor was cleaved in all conditions tested and appeared as two bands at ~45kDa and ~43kDa.

161   These bands were compatible with the molecular weight of Aquamarine + LC3B-I at ~45 kDa, and of

162   Aquamarine + LC3B-II at ~43 kDa (Fig. 1E). Consistent with the quantifications of puncta numbers in cells

163   expressing the WT biosensor (Fig. 1B, C), the levels of the Aqua-LC3B-II band increased upon BafA$_1$ or

164   Torin1 treatment, but remained unaltered upon starvation with HBSS (Fig. 1E, F). A further increase in Aqua-

165   LC3B-II abundance was observed upon the co-treatment with BafA$_1$ and Torin1 when compared to BafA$_1$ or

166   Torin1 alone (Fig. 1E, F). Similarly, the combination of HBSS and BafA$_1$ increased the levels of Aqua-LC3B-

167   II when compared to HBSS alone (Fig. 1E, F). These findings suggest a rather rapid degradation of Aqua-

168   LC3B-II via lysosomal turnover in U2OS cells upon starvation with HBSS. This also suggests that the

169   degradation of Aqua-LC3B-II can be slowed down when starvation is coupled with a late-stage lysosomal

170   inhibitor such as BafA$_1$. This was previously reported to occur in several other cell lines [24,40,41], and it

171   substantiates the importance of measuring the autophagy flux in the absence or presence of lysosomal

172   inhibitors. The differences observed in the levels of Aqua-LC3B-II were also observable at the level of the

173   endogenous LC3B-II, confirming that the lipidation levels of the LC3B biosensor are similar to those of

174   endogenous protein upon autophagy induction and/or lysosomal inhibition (Fig. 1E, G).

175   To explore whether a portion of Aqua-LC3B-II puncta structures are capable of colocalizing with

176   lysosomes, we analyzed their juxtaposition with the lysosomal protein Lysosomal Associated Membrane

177   Protein 2 (LAMP2). Compared to control cells, we found that the colocalization of Aqua-LC3B-II puncta

structures with LAMP2-positive objects significantly increased when autophagy is induced with Torin1, but not with HBSS (Fig. 1B, D). As expected in cells expressing the WT biosensor, we observed that treatment with BafA$_1$ significantly reduced the colocalization of Aqua-LC3B-II puncta with LAMP2 compared to untreated, Torin1- or HBSS-treated cells. Conversely, the G120A biosensor did not colocalize with LAMP2 in any condition (Fig. 1D and S1). Overall, these results show that the WT biosensor colocalizes with LAMP2 in an autophagy-dependent manner.

Taken together, these results demonstrate that the LC3B biosensor is efficiently cleaved. The biosensor is capable of forming puncta structures that are consistent with the lipidated, Aqua-LC3B-II form, and they colocalize with the lysosomal protein LAMP2. The autophagy-dependent changes in the number of puncta-shaped structures or their degree of colocalization with LAMP2 indicate that the biosensor is capable of successfully reporting on autophagy induction and/or lysosomal inhibition.

The LC3B biosensor responds to the changes in proLC3B priming in an ATG4B-dependent manner

After establishing that the biosensor behaves like endogenous LC3B in cells, we sought to assess its capacity to dynamically report on LC3B processing. To this end, live cells expressing the WT or the uncleavable G120A biosensor were analyzed using FRET/FLIM. We compared the donor (Aquamarine) lifetime differences between the donor-only and the biosensor to detect FRET events, which are highlighted when the donor lifetime decreases. We then used ΔLifetime as a readout for FRET/FLIM analyses, which was determined by calculating the net difference between the lifetime of the donor-only construct (Aquamarine-proLC3B) and that of a biosensor (either Aquamarine-proLC3B- or proLC3B^{G120A}-tdLanYFP). We hypothesized that a positive ΔLifetime would be indicative of a FRET event between Aquamarine and tdLanYFP, therefore corresponding to the presence of unprimed proLC3B.

First, we measured the FRET/FLIM readout of the WT biosensor by calculating its mean ΔLifetime in the total cell area. This includes the cytosol and the puncta structures, in which the precursor, primed and lipidated forms of LC3B are expected to be present. We observed that no FRET was occurring in control cells, as illustrated by a ΔLifetime difference close to zero (Fig. 2A, B). This indicates that the LC3B biosensor is

completely primed under basal conditions, leading to the loss of the tdLanYFP moiety. Conversely, the uncleavable G120A biosensor reported a significant increase of ~500 psec in ΔLifetime compared to the WT biosensor. This led us to conclude that the FRET readout of the LC3B biosensor is directly linked to its cleavage on G120. In addition, the FRET readout is specific to the biosensor constructs, as we observed no difference in ΔLifetime between the WT and G120A donor-only constructs (Fig. S2A, B).

We then reasoned that the direct correlation between FRET and priming should make the LC3B biosensor responsive to the presence or absence of ATG4. To this end, we used siRNA-mediated gene silencing to downregulate the *ATG4B* isoform, as it exhibits the highest catalytic efficiency towards LC3B compared to the other members of the ATG4 family [42]. First, we verified the efficiency of the siRNA-mediated downregulation strategy by western blotting, in cells expressing the WT or the G120A biosensor (Fig. S2C, D). When comparing the mean ΔLifetime values, no difference was observed in cells expressing the G120A biosensor under any condition, as expected (Fig. 2A, B). Although no difference in mean ΔLifetime was observable in control or *ATG4B*-depleted cells expressing the WT biosensor (Fig. 2A, B), we noticed the presence of a significant subset of pixels exhibiting high ΔLifetime values only in *ATG4B*-depleted cells (Fig 2A, enlarged ΔLifetime image of the WT biosensor with *ATG4B* siRNA). Therefore, we hypothesized that these pixels might correspond to unprimed proLC3B. To verify our hypothesis, we ascertained that these pixels could be retrieved only upon *ATG4B* downregulation, and that they could represent unprimed pools of LC3B by showing a G120A-like FRET. To this end, we performed a pixel-by-pixel FRET/FLIM analysis to quantify the number of pixels showing ΔLifetime values similar or higher than the mean ΔLifetime of the G120A biosensor. Indeed, *ATG4B* silencing caused a significant increase in the number of pixels with high ΔLifetime values compared to the control condition (Fig. 2C). We then used the power of FRET microscopy to visualize these high ΔLifetime pixels with a line analysis. This analysis allows to observe the local variations in ΔLifetime occurring in the pixels crossed by a straight line. ΔLifetime values along the line went from zero to the levels of the G120A biosensor only in cells silenced for *ATG4B* (Fig. 2A, D). This indicates a lack of proLC3B cleavage occurring locally, and it substantiates the role of ATG4B in this process. We also noticed

228   that the increase in ΔLifetime was localized in pixels found on or near the puncta-shaped structures (Fig. 2A).

229   This reveals the spatial heterogeneity of the priming activity in these areas and uncovers a possible spatial

230   regulation of proLC3B priming, which may be taking place in discrete regions in the vicinity of

231   autophagosomes. When we performed the same analysis for donor-only constructs, we could not detect any

232   high ΔLifetime pixels, ensuring that the effect that we observe with the WT biosensor upon *ATG4B*

233   downregulation was not due to an intrinsic change in the lifetime properties of Aquamarine (Fig. S2E). To

234   make sure that the heterogeneity of ΔLifetime pixels was correctly estimated in the different conditions, we

235   analyzed the data to visualize the ΔLifetime distribution. We hypothesized that the presence of high ΔLifetime

236   pixels with G120A biosensor-like ΔLifetime values should change the overall ΔLifetime distribution. To this

237   end, we superimposed the histograms of the cells expressing the WT biosensor with or without *ATG4B*

238   depletion, and we observed a shift in the histogram mode values of *ATG4B*-depleted cells towards higher

239   ΔLifetime values (Fig. 2E). Since the mode value of a histogram corresponds to the value with the highest

240   frequency, a positive shift in the mode indicates that the ΔLifetime distribution changes due to the presence

241   of FRET events in the biosensor.

242   We then sought to verify whether FRET events in *ATG4B*-depleted cells were specific to the presence

243   of proLC3B pools in discrete locations, or whether they were due to the clustering of the cleaved reporter. We

244   reasoned that if FRET is due to the unspecific proximity of donor and acceptor molecules, high-ΔLifetime

245   pixels should also be visible when the donor and the acceptor are expressed on distinct LC3B molecules. To

246   rule out this possibility, we compared the FRET behavior of the cells expressing the biosensor with the cells

247   co-expressing the donor and the acceptor constructs [donor-only (Aquamarine-proLC3B) + acceptor-only

248   (proLC3B-tdLanYFP)]. Similar to the WT biosensor, the mean ΔLifetime values of cells co-expressing donor

249   + acceptor in the presence of a control siRNA were close to zero, and no further change was observed upon

250   *ATG4B* downregulation (Fig. S3A-B). Sensitive analyses revealed that donor + acceptor co-expressing cells

251   did not exhibit any high-ΔLifetime pixels when *ATG4B* was depleted, while such high-ΔLifetime pixels were

252   detectable in cells expressing the biosensor (Fig. S3C). As shown in Fig. 2D, *ATG4B* depletion induced a local

253 increase in ΔLifetime values in the proximity of puncta in cells expressing the biosensor (Fig. S3D), and an

254 increase in histogram mode value (Fig. S3E). However, these changes were absent in donor + acceptor co-

255 expressing cells (Fig. S3D, E). These drastic differences in the FRET response of the cells co-expressing the

256 donor and the acceptor compared to the LC3B biosensor strongly suggest that FRET events are intramolecular

257 and specific to the biosensor construct, and they are intimately linked to its priming by ATG4B.

258   Considering that, in addition to its priming activity, ATG4B also acts as a deconjugating enzyme that

259 governs the ATG8ylation levels [25,43], we checked if its depletion is causing an increase in the puncta-

260 shaped structures. In cells expressing the WT biosensor or donor, we observed a robust increase in the number

261 of LC3B puncta upon *ATG4B* downregulation compared to controls (Fig. 2F, S2F). This indicates that the

262 formation of puncta-shaped structures depends on the presence of ATG4B. As expected, no puncta were

263 observed in cells expressing the G120A biosensor or donor, regardless of the presence or absence of ATG4B

264 (Fig. 2F, S2F). Similarly, when we analyzed protein levels by western blotting, we detected a significant

265 increase in the lipidated levels of the biosensor (Aqua-LC3B-II) and of the endogenous LC3B-II upon *ATG4B*

266 downregulation, compared to the controls (Fig. S2C, D).

267   Taken together, these results show that the LC3B biosensor allows to visualize changes in the ATG4B-

268 dependent priming of proLC3B. We provide evidence that the biosensor can form LC3B puncta in an ATG4B-

269 dependent manner, demonstrating that our probe recapitulates the key features of endogenous LC3B. Last, we

270 demonstrate that analyzing the FRET response of the biosensor with different modalities allows to monitor

271 the cleavage of proLC3B both at the cellular and at the subcellular level. Our findings support the pertinence

272 of this tool to spatiotemporally characterize LC3B processing in cells.

273

The total depletion of ATG4B maximizes the FRET response of the LC3B biosensor

275 To deepen our understanding of the mode of action of the LC3B biosensor in cells, we used *ATG4* knockout

276 (KO) HeLa cells generated by Agrotis *et al.* using CRISPR/Cas9-mediated approaches [24]. First, we

277 measured the FRET response of the WT or G120A biosensor expressed in control cells. Similarly to what

278   observed in U2OS cells (Fig. 2A, B), the WT biosensor displayed a ΔLifetime close to zero, while the FLIM

279   readout of the cleavage-deficient G120A biosensor showed a ~400 psec ΔLifetime (Fig. 3A, B). When looking

280   at the distribution of the two sensors, we observed that the WT biosensor was capable of forming puncta-like

281   structures while the G120A biosensor showed a cytosolic distribution as expected (Fig. 3A). Overall, the

282   FRET behavior and the distribution of the WT and G120A LC3B biosensors were consistent with our previous

283   observations in U2OS cells.

284   We then sought to explore the FRET/FLIM readout of the LC3B biosensor in cells completely devoid

285   of the ATG4 protease. We expressed the WT biosensor in *ATG4B* single knockout (SKO) HeLa cells and in

286   comparison to control cells, the WT biosensor displayed mean ΔLifetime values of ~400 psec under these

287   conditions (Fig. 3A, B). These values were nearly identical to the mean ΔLifetime of the G120A biosensor.

288   Similarly to the distribution of the G120A biosensor, the WT biosensor in SKO cells did not exhibit noticeable

289   puncta-like structures, and it remained cytosolic. Therefore, these findings support the loss of priming of the

290   WT biosensor in an *ATG4B* SKO background. The lack of priming of the LC3B biosensor was also evident

291   in western blotting analyses (Fig. S4). The WT biosensor expressed in control cells displayed two bands

292   corresponding to the primed and the lipidated forms of the probe, both in the ~43-45 kDa range. In contrast,

293   the WT biosensor expressed in *ATG4B* SKO cells exhibited a single band at ~95 kDa. This band is similar to

294   that observed in cells expressing G120A biosensor, therefore reinforcing the conclusion that the WT biosensor

295   remains unprimed in cells lacking the ATG4B protease. We observed that the complete knockout of *ATG4B*

296   also abolishes the priming of endogenous LC3B, which exhibits a single band at 15 kDa compatible with

297   unprimed proLC3B [44] (Fig. S4). These results indicate that ATG4B is indispensable for the priming and the

298   lipidation of the LC3B biosensor.

299   We then verified whether the A and C isoforms of ATG4 family could further contribute to the priming

300   of the LC3B biosensor. The mean ΔLifetime values (Fig. 3A, B) and the western blotting profiles (Fig. S4) of

301   the WT biosensor expressed in *ATG4A/B* double knockout (DKO) or *ATG4A/B/C* triple knockout (TKO) HeLa

302   cells [24] showed no differences compared to the *ATG4B* SKO condition. This substantiates previous *in vitro*

303 reports showing that the catalytic activity of ATG4B is maximized towards LC3B [45]. To rule out every

304 possibility that the A or C isoforms could still contribute to the priming of LC3B to some extent, we increased

305 the sensitivity of our analyses by performing pixel-by-pixel FRET/FLIM calculations. We quantified the

306 number of pixels with ΔLifetime values similar or higher than the ΔLifetime of the G120A biosensor in

307 control, *ATG4B* SKO, *ATG4A/B* DKO or *ATG4A/B/C* TKO cells. With this, we aimed to explore subtle

308 changes possibly occurring between the KO cells that may remain undetected in mean ΔLifetime analyses. As

309 expected, we observed a significant increase in the number of pixels with high ΔLifetime in *ATG4B* SKO cells

310 expressing the LC3B biosensor when compared to control cells, further corroborating the results obtained with

311 mean ΔLifetime analyses (Fig. 3C). However, these analyses did not highlight any significant increase in the

312 number of pixels with high ΔLifetime upon further loss of *ATG4A* or *ATG4C* (Fig. 3C) although we noted that

313 *ATG4A/B* DKO and *ATG4A/B/C* TKO cells showed a slight shift towards higher ΔLifetime values in their

314 respective histogram mode value compared to the mode value of *ATG4B* SKO cells (Fig. 3D).

315 Similarly to what observed for the endogenous LC3B protein, our results demonstrate that the priming

316 of the LC3B biosensor is highly dependent on the presence of ATG4B. When *ATG4B* is absent, the LC3B

317 biosensor displays a significant FRET response, it remains unprimed and cannot be lipidated to form puncta-

318 like structures, overall resembling the behavior of the cleavage- and lipidation-deficient G120A biosensor.

319

The ectopic expression of active ATG4B rescues the priming deficiency of the LC3B biosensor in ATG4B-

deficient cells

322 After demonstrating that the priming of the LC3B biosensor is ATG4B-dependent, we then asked whether its

323 FRET response in ATG4B-deficient cells could be rescued by re-expressing ATG4B. To this end, we co-

324 expressed the LC3B biosensor together with an empty vector or with a vector coding for WT ATG4B. Then,

325 we evaluated the FRET/FLIM behavior of these conditions both in control and in *ATG4B* SKO cells.

326 Consistent with our previous findings (Fig. 3), the LC3B biosensor co-expressed with an empty vector in

327 *ATG4B* SKO cells showed a significant increase in its mean ΔLifetime values compared to control cells (Fig.

328 4A, B). Conversely, the expression of WT ATG4B in *ATG4B* SKO cells caused a drastic decrease in the mean

329 ΔLifetime values of the LC3B biosensor, which were close to zero. This suggests that the reintroduction of

330 WT ATG4B is sufficient to fully rescue the cleavage of the LC3 biosensor in a SKO background. Upon the

331 expression of exogenous ATG4B in control cells, we also observed that the distribution of the biosensor was

332 cytosolic and without significant puncta-like structures (Fig. 4A). On the contrary, control cells co-expressing

333 an empty vector were capable of forming puncta-like structures. This is in agreement with previous reports

334 showing that the overexpression of exogenous ATG4B blocks the lipidation of LC3B and by doing so, it leads

335 to the disappearance of LC3-positive puncta in cells [13,46,47].

336 Next, we assessed whether two mutant forms of ATG4B with different catalytic activities could rescue

337 the priming deficiency of the LC3B biosensor in *ATG4B* SKO cells. We first explored the consequences of

338 mutating the Cys74 residue of ATG4B into Ser (C74S). Cys74 belongs to a group of three aminoacids known

339 as the "catalytic triad", and its mutation into Ala or Ser was shown to cause a complete loss of the catalytic

340 activity of ATG4B [13,35]. When ATG4B^{C74S} was co-expressed with the LC3B biosensor in *ATG4B* SKO

341 cells, we measured a mean ΔLifetime comparable to *ATG4B* SKO cells transfected with an empty vector (Fig.

342 4A, B). This indicates that the catalytically-dead C74S mutant was unable to cleave and, by consequence

343 prime, the LC3B biosensor. We then tested a second mutant form of ATG4B where Trp142 was mutated into

344 Ala (W142A). Trp142 is one of the residues surrounding the catalytic triad, and its mutation into Ala was

345 reported to significantly reduce the catalytic activity of ATG4B *in vitro* [35]. Surprisingly, we observed that

346 ATG4B^{W142A} behaved similarly to WT ATG4B when expressed in SKO cells, and it resulted in a complete

347 cleavage of the LC3B biosensor in FRET/FLIM analyses (Fig. 4A, B). This supports the superior catalytic

348 efficiency of ATG4B to prime proLC3B in living cells, even in conditions where its catalytic activity is

349 severely compromised by the W142A mutation. To verify that these changes in mean ΔLifetime were specific

350 to the LC3B biosensor, we analyzed the mean ΔLifetime profiles of control or *ATG4B* SKO cells expressing

351 the donor-only Aquamarine-LC3B construct together with WT, C74S or W142A ATG4B (Fig. S5A). As

352 expected, we did not observe any difference among all the conditions tested, further confirming that the mean

353 ΔLifetime FRET/FLIM readout is specific towards the ATG4B-mediated cleavage of the LC3B biosensor.

354 We then wanted to verify if our approach based on mean ΔLifetime was sensitive enough to conclude

355 on the capacity of the W142A mutant to fully prime LC3B. Therefore, we further evaluated the readout of the

356 LC3B biosensor by performing pixel-by-pixel FRET/FLIM calculations, which we previously showed to be

357 more sensitive than mean ΔLifetime analysis (Fig. 2). As expected, we observed a significant increase in the

358 number of pixels with high ΔLifetime – indicating no LC3B priming – in *ATG4B* SKO cells co-expressing an

359 empty vector or ATG4B^{C74S} compared to control cells (Fig. 4C). Similarly to mean ΔLifetime analyses (Fig.

360 4B), expressing WT ATG4B or ATG4B^{W412A} in *ATG4B* SKO cells revealed an absence of pixels with high

361 ΔLifetime values, suggesting a complete rescue of the priming activity of the LC3B biosensor with both

362 constructs (Fig. 4C). Accordingly, the histogram analyses of the distribution of FRET pixels in all conditions

363 showed almost identical mode values in *ATG4B* SKO cells co-expressing WT or ATG4B^{W142A}, with their

364 respective mode values centered around zero (Fig. 4D). On the contrary, the mode values of *ATG4B* SKO

365 cells expressing an empty vector or ATG4B^{C74S} were drastically shifted towards 400 psec, which is again

366 indicative of significant FRET (Fig. 4D). As expected, the analysis of the high ΔLifetime pixels in control or

367 SKO cells expressing the donor-only Aquamarine-LC3B and each of the ATG4B constructs did not reveal

368 any difference (Fig. S5B). Again, this substantiates the specificity of our different FRET/FLIM readouts for

369 the LC3B biosensor only. In addition to this, the WT biosensor expressed in control cells with each of the

370 ATG4B constructs exhibit similar histogram mode values (Fig. S5C). Nevertheless, we observed the presence

371 of a shoulder corresponding to ΔLifetime values of ~200-300 psec in control cells co-expressing the WT

372 biosensor with ATG4B^{C74S} (Fig. S5C), which could reflect the previously reported dominant negative effects

373 of ATG4B^{C74S} on the soluble forms of LC3B [46].

374 Finally, to rule out if the capacity of WT or mutant ATG4Bs to prime proLC3B can differ due to

375 changes in their expression levels, we performed western blotting analyses to compare exogenous ATG4B

376 protein levels and their proLC3B priming patterns. We first verified that protein expression levels of

377   overexpressed WT or mutant ATG4Bs in control or *ATG4B* SKO cells were comparable (Fig. S5D). Then,

378   we confirmed that *ATG4B* SKO cells co-expressing WT or ATG4B^{W142A} but not ATG4B^{C74S} exhibited bands

379   compatible with the molecular weight of Aquamarine + LC3B-I at ~45 kDa. On the hand, *ATG4B* SKO cells

380   co-expressing ATG4B^{C74S} only exhibited a higher molecular weight band compatible with the size of

381   Aquamarine + proLC3B + tdLanYFP (Fig. S5D).

382   Altogether, our results demonstrate that the proLC3B priming deficiency observed in *ATG4B* SKO

383   cells can be fully restored when co-expressing the WT or W142A forms of ATG4B, but not with the

384   catalytically-dead C74S. Although ATG4B^{W142A} was shown to display a reduced catalytic activity *in vitro*

385   [35], we demonstrate that this mutant is able to prime proLC3B in living cells similar to WT ATG4B. These

386   data were obtained with three independent methods to calculate the FRET behavior of the LC3B biosensor

387   and with an orthogonal approach based on western blotting analyses. Together, they provide novel insights on

388   the superior capacity of ATG4B to prime LC3B *in cellulo* even in conditions where its catalytic activity is

389   compromised. Importantly, they also support the notion that the catalytic activity of ATG4B needs to be

390   completely eliminated to abolish LC3B priming.

391

392   *The LC3B biosensor reveals the mode of action of ATG4 inhibitors in cells*

393   Given that the biosensor reports on the priming of LC3B by ATG4B, we sought to investigate whether it is

394   also capable to respond to pharmacological compounds that inhibit the ATG4B-LC3B axis. We first explored

395   the readout of the LC3B biosensor on commercially-available inhibitors of ATG4s. Tioconazole, LV-320,

396   FMK-9a, NSC 185058 (NSC) and *Z-L*-Phe chloromethyl ketone (ZPCK) were evaluated in their capacity to

397   inhibit the priming and/or deconjugation activities of ATG4B [48–53]. These inhibitors have either been

398   synthesized or identified in screening studies, and they were previously shown to inhibit ATG4B and/or other

399   ATG4 isoforms. They were also reported to have a significant therapeutic potential in chemotherapy-resistant

400   cancer subtypes with elevated levels of autophagy [29,30].

401   We determined the working concentration of LV-320, FMK-9a and NSC based on previous reports

402 testing the effects of these compounds in cells [49,51,52]. For Tioconazole, we decreased the concentration

403 (to 4 µM) as we experienced high rates of cell death when using the compound at the previously reported

404 concentration (40 µM) [48]. Finally, for ZPCK, we determined a dose that can be tolerated by our cells and

405 based on available IC_{50} values determined by different assays [53]. Since the reported concentrations are

406 different according to the compound used, we then chose to standardize the duration of the treatment to 6

407 hours to be able to detect short- to mid-term effects of each compound. After determining the dose and the

408 duration to be tested, we first measured the mean ΔLifetime values in HeLa cells expressing the WT or the

409 G120A biosensor, and treated or not with each of the five inhibitors. When cells are treated with the inhibitors,

410 we expected to observe a FRET response compatible to that detected in cells downregulated for *ATG4B* as the

411 available reports demonstrated the effects of ATG4 inhibitors mostly inhibiting the deconjugation activity

412 with limited impact on the priming activity [48,49,51,52],. Within our selected set of inhibitors, two of them

413 – NSC and ZPCK – were found to significantly increase mean ΔLifetime values compared to controls (Fig.

414 5A vs. 5E, F). On the contrary, Tioconazole, LV-320 and FMK-9a did not alter the mean ΔLifetime values of

415 the biosensor (Fig. 5A-D). However, the mean ΔLifetime values of cells treated with NSC or ZPCK remained

416 lower than those of cells expressing the G120A biosensor. This suggests that the inhibitory effect of these

417 drugs towards ATG4B remains partial. We then asked whether the main function of NSC and ZPCK is to

418 inhibit the ATG4B-dependent deconjugation of LC3B or its priming. We observed a significant increase in

419 the number of Aqua-LC3B-II puncta structures upon treatment with NSC or ZPCK, further supporting the

420 idea that autophagy can still be triggered in the presence of these compounds and that the inhibition of ATG4B

421 priming activity is not complete (Fig. 5E, F). However, increased levels of Aqua-LC3B-II puncta structures

422 were observed in cells treated with Tioconazole, LV-320 or FMK-9a as well (Fig. 5B-D), and we found no

423 correlation between puncta numbers and mean ΔLifetime values with any of the inhibitors (Fig. S6). These

424 findings suggest that all the tested compounds preferentially hinder the deconjugation activity of ATG4B

425 towards LC3B, which was described to be more sensitive to ATG4B inhibition than the priming activity [54].

426   In addition to deconjugation, mean ΔLifetime differences provide the first evidence that NSC and ZPCK also

427   inhibit the priming activity of ATG4B.

428   To dissect the efficacy of the five ATG4B inhibitors with methods allowing for greater sensitivity than

429   mean ΔLifetime, we then performed high ΔLifetime-pixel counting and histogram analyses. The high

430   ΔLifetime-pixel counting analyses revealed that not only NSC and ZPCK, but also FMK-9a exhibited a

431   significantly increased number of pixels with high ΔLifetime compared to control cells (Fig. 6A-D). We also

432   performed western blotting analyses to investigate if proLC3B accumulation can be observed upon treatment

433   with ATG4B inhibitors. In line with FRET results, we observed bands at a molecular weight compatible with

434   the unprimed biosensor (Aqumarine + proLC3B +tdLanYFP) only in cells treated with FMK-9a, NSC or

435   ZPCK but not in cells treated with Tioconazole or LV-320 (Fig. S7). However, we also noticed that the

436   proLC3B band is more abundant in cells treated with FMK-9a or NSC compared to cells incubated with

437   ZPCK. Although inhibitors were added in all steps of sample preparation to avoid proLC3B priming at any

438   moment, it is likely that the differences observed in the abundance of proLC3B bands is due to the differential

439   efficacy of the compounds used under denaturing conditions. Therefore, these results further substantiate the

440   importance of quantitative assays performed with living cells when investigating the efficacy of potential

441   ATG4B inhibitors. Indeed, when we analyzed the distribution of ΔLifetime pixels on histogram analyses, we

442   observed that approximately 10-20% of pixels in cells treated with NSC or ZPCK were exhibiting G120A

443   biosensor-like ΔLifetime values (Fig. 6A-D). These values were lowered in the presence of Tioconazole, LV-

444   320 and FMK-9a, further corroborating the superiority of NSC and ZPCK in inhibiting ATG4B (Fig. S8). In

445   line with these findings, histogram analyses revealed that NSC (113 psec) and ZPCK (150 psec) have the

446   largest histogram mode value shift from that of control cells (Fig. 6C, D). Interestingly, these analyses showed

447   that FMK-9a, Tioconazole and LV-320 also display a mode value shift from that of control cells, respectively

448   of 74, 65 and 47 psec (Fig. 6B and S8B-C). Therefore, this sensitive analysis method indicates a mild inhibition

449   of the priming activity of ATG4B by FMK-9a, Tioconazole and LV-320 as well, which was undetectable with

450 the other analysis methods. Furthermore, this approach substantiates the superior capacity of NSC and ZPCK

451 in inhibiting ATG4B.

452 Since we observed the presence of high ΔLifetime pixels with all the inhibitors, we then sought to

453 investigate the subcellular location of these pixels using line analysis. Similarly to what observed on cells

454 silenced for *ATG4B* (Fig. 2), we noticed that high ΔLifetime pixels were located either on the puncta-shaped

455 structures, or in the surrounding area (Fig. 6 and S8). Line analyses also revealed that these pixels had

456 ΔLifetime values comparable to those of the G120A biosensor, regardless of the compound used. Taken

457 together, these findings show that ATG4B inhibition using commercially-available drugs reduces the priming

458 rates of proLC3B at discrete sites, where unprimed LC3B reservoirs can be found within or in the proximity

459 of puncta-shaped structures.

460 Afterwards, we explored the effect of MG132, a peptide aldehyde that inhibits both the proteasome

461 and cysteine proteases [55,56]. Considering that ATG4B is a cysteine protease [14,35], we reasoned that

462 MG132 might be able to block its catalytic activity towards LC3B. However, its inhibitory capacity towards

463 ATG4B has never been explored. Therefore, we used our FRET pipeline to explore the efficacy of an inhibitor

464 with unknown effects towards ATG4B. Therefore, we treated HeLa cells expressing the WT or G120A

465 biosensor with DMSO or MG132, and calculated their mean ΔLifetime (Fig. S9A, B). FLIM analyses revealed

466 a significant increase in the mean ΔLifetime values of the WT biosensor in the presence of MG132. We

467 reasoned that MG132 could promote FRET within the biosensor either by inhibiting the priming activity of

468 ATG4B, or by inhibiting LC3B degradation by the proteasome. To distinguish between these two possibilities,

469 we relied on the subcellular distribution of the biosensor. In this light, the biosensor should be retrieved in the

470 cytosol in case MG132 had mainly an ATG4B-specific inhibition on proLC3B priming. Alternatively, it

471 should rather be found in puncta-like structures if this drug acted as a proteasome inhibitor. We observed a

472 significant increase in the number of Aqua-LC3B-II puncta-like structures in cells expressing the WT

473 biosensor and treated with MG132, when compared to DMSO-treated cells (Fig. S9B). Therefore, this

474 localization of the sensor in puncta-like structures suggests that MG132 is more efficient as a proteasome

475 inhibitor, rather than a specific ATG4B inhibitor. Although the number of pixels with high ΔLifetime values

476 did not significantly increase upon MG132 treatment (Fig. S9B), the histogram analysis of MG132-treated

477 cells expressing the WT biosensor revealed a mode value change when compared to DMSO-treated cells and

478 to cells expressing the G120A biosensor (Fig. S9C). Overall, this indicates that G120A-like FRET events are

479 quantitatively modest in the presence of MG132, suggesting that MG132 preferentially acts as a proteasomal

480 inhibitor rather than an ATG4B-specific inhibitor. Although G120A-like FRET events were limited under

481 these conditions, we sought to explore their spatial localization. Line analyses performed in cells expressing

482 the WT biosensor and treated with MG132 revealed that the ΔLifetime variations of the biosensor were of

483 ~200 psec in the cytosol, and reaching ΔLifetime values of the G120A biosensor (~400 psec) on or near the

484 LC3B puncta (Fig. S9B, D). In contrast, no fluctuations were observed in the cytosol or near puncta in control

485 cells. These two FRET values observed after treating cells with MG132 could be recapitulative of the dual

486 action of this compound: a modest ATG4B inhibitor keeping the biosensor in the cytosol, and a more potent

487 proteasomal inhibitor on LC3B-positive puncta. Of note, since Aqua-LC3B can efficiently localize on puncta-

488 like structures (Fig. S9B) which display high FRET (Fig. S9B, D), our data raise the possibility that MG132

489 does not alter the cleavage of tdLanYFP from the biosensor. It is possible that the inhibition of proteasomal

490 activity impairs the degradation of the FRET acceptor, thereby allowing for non-specific FRET events. Indeed,

491 western blotting of cells treated with MG132 exhibited no band that may be compatible with the size of the

492 unprimed biosensor (Fig. S9E). Therefore, these results underline the importance of performing spatially-

493 resolved, pixel-by-pixel FRET calculations to understand where and to what extent the biosensor is active.

494 Last, they also highlight the poor efficacy of MG132 as an ATG4B-specific inhibitor.

495

496 Overall, our data demonstrate that the LC3B FRET biosensor is a powerful tool to evaluate the mode

497 of inhibition of ATG4B-specific compounds. We also provide an innovative methodology where individual

498 sets of microscopy data can be analyzed using three independent approaches. Cumulating the information

499 obtained by the three approaches allows to spatially localize and quantify the ATG4B-dependent priming and

500 deconjugation of LC3B with unprecedented precision, and it is mandatory to characterize the mode of action

501 of present and future ATG4B-specific inhibitors.

502

The LC3B biosensor uncovers the CDK1-dependent regulation of the ATG4B-LC3B axis at mitosis

504 Given the sensitivity of our biosensor to monitor autophagy within the ATG4B-LC3B axis, we sought to

505 explore the involvement of this nexus in a paradigm relevant for cell physiology. In this light, we assessed the

506 FRET behavior of the LC3B biosensor at mitosis, a cell cycle phase where the involvement of autophagy is

507 still controversial. Although autophagy was described to be turned off during cell division [57–59], numerous

508 studies reported the presence of LC3B-positive puncta in mitotic cells [60–62], and the role of ATG4B in this

509 cell cycle phase and on those puncta has never been elucidated. As we uncovered the presence of unprimed

510 LC3B pools on or in the close vicinity of puncta-shaped structures upon *ATG4B* downregulation or ATG4B

511 inhibition, we asked whether mitotic LC3B puncta could be discrete sites containing unprimed LC3B. To this

512 end, we first compared the FRET response of the WT biosensor between interphase cells (unsynchronized),

513 and cells arrested at G2/M following treatment with nocodazole and then released to reach metaphase. When

514 compared to cells expressing the G120A biosensor, the mean ΔLifetime values of the WT biosensor both in

515 unsynchronized and in nocodazole-treated cells were close to zero (Fig. 7A-B). Though LC3B puncta-shaped

516 structures were present in mitotic cells as previously reported [60–62], high-ΔLifetime pixel analyses revealed

517 that proLC3B-like pixels were absent in these cells (Fig. 7C). Line analysis, on the other hand, identified local

518 ΔLifetime variations of ~200 psec on or around the puncta of nocodazole-treated mitotic cells (Fig. 7D). These

519 events were quantitatively modest in number, as the histogram mode value of mitotic cells following

520 nocodazole-mediated synchronization fluctuates around zero (Fig. 7E). Altogether, these results suggest that

521 LC3B is mainly cleaved in mitotic cells, and that the mitotic repression of autophagy is not related with the

522 accumulation of proLC3B pools.

523 In a recent study published by Odle *et al.*, it has been shown that CDK1 ensures the mitotic repression

524 of autophagy by replacing mTORC1-dependent inhibitory phosphorylations on autophagy regulator proteins

21

525 such as ATG13, ULK1, ATG14 and TFEB [63]. This report also showed that the treatment of mitotic cells

526 with the CDK1 inhibitor RO-3306 reversed the inhibitory phosphorylations on autophagy regulator proteins.

527 However, it is currently unknown whether CDK1 inhibition also plays a role within the ATG4B-LC3B axis

528 at mitosis, potentially by regulating the ATG4B-dependent proLC3B processing. To this end, we synchronized

529 U2OS cells at mitosis with nocodazole and we inhibited CDK1 with RO-3306. First, we confirmed the efficacy

530 of CDK1 inhibition, using the activation of the cell cycle protein AURKA as a readout. Indeed, AURKA was

531 shown to be activated on Thr288 at mitosis in a CDK1-dependent manner [64]. Therefore, we used our FRET

532 biosensor reporting on AURKA activation [39] to explore the effect of RO-3066 at mitosis. With this tool, we

533 observed that the mitotic spindle failed to form correctly in U2OS cells synchronized at mitosis and treated

534 with RO-3066 (Fig. S10A). This is comparable to what observed with a kinase-dead mutant of the AURKA

535 biosensor in previous reports [38,39], indicating mitotic defects compatible with a failure in activating

536 AURKA [64]. As expected, the FRET readout of the AURKA biosensor revealed a lowered activation of

537 AURKA in cells treated with RO-3066 (Fig. S10A-B). After confirming that CDK1 is inhibited under our

538 experimental conditions, we explored the FRET readout of the LC3B biosensor in cells synchronized at

539 mitosis and in the presence or absence of RO-3306. Although we noticed a trend towards higher mean

540 ΔLifetime values in nocodazole and RO-3306 co-treated cells as compared to either unsynchronized or

541 nocodazole-only treated cells, this trend was not significant (Fig. 7A-B). Similarly, the sensitive high-

542 ΔLifetime pixel analyses did not reveal any significant changes in nocodazole and RO-3306 co-treated cells

543 when compared to unsynchronized or nocodazole-only treated cells (Fig. 7C). However, line analyses showed

544 ~100/200 psec local ΔLifetime variations (Fig. 7D). These differences were abundant in number, since the

545 histogram mode value of nocodazole and RO-3306 co-treated cells shifted towards high ΔLifetime values

546 (Fig. 7E). This increase suggests a CDK1-dependent stalling of the proLC3B processing rates by ATG4B.

547 Overall, these results uncover the role of CDK1 in regulating the ATG4B-LC3B axis at mitosis. In addition,

548 they further highlight the superior sensitivity of the LC3B biosensor to explore subtle changes in the regulation

549 of autophagy, and particularly in paradigms where the role of the ATG4B-LC3B axis still remains to be

550 determined.

551

Discussion

553 In this study, we demonstrated that the LC3B biosensor is a robust tool to monitor autophagy, as it responds

554 to the priming and deconjugation activities of ATG4B on LC3B. We showed that these functions of ATG4B

555 can be followed by using one single probe with a dual readout based on FRET, and on the accumulation of

556 the probe on autophagosomes.

557   Among the several approaches available to monitor autophagy, the most widely used assays rely on

558 the use of single fluorescent protein (FP)-tagged LC3B probes to quantify the number of autophagosomes

559 [65]. The LC3B biosensor retains this property, since it functions as a standard single FP-tagged probe after

560 LC3B is primed. We also show that the biosensor reports on autophagy induction and/or inhibition while

561 colocalizing with the lysosomal marker protein LAMP2 in an autophagy-dependent manner, similarly to other

562 LC3B-based fluorescent constructs. Since the LC3B biosensor is constituted of a pair of FPs resistant to acidic

563 pH, its readout can be followed throughout the entire autophagy pathway. Importantly, the LC3B biosensor

564 has the capacity to respond to proLC3B priming in living cells, thanks to these FPs behaving as a donor-

565 acceptor FRET pair. The proLC3B priming by ATG4s is among the earliest events occurring when autophagy

566 is triggered [13,36]. A FRET-based strategy relying on a CFP/YFP donor-acceptor pair has already been used

567 to measure the enzymatic activity of ATG4A and ATG4B towards the ATG8 family in a purely *in vitro* system

568 [66]. However, this strategy has never been implemented in living cells, most likely due to the lack of yellow

569 FPs retaining their acceptor properties in conditions of acidic pH. The recent development of tdLanYFP [39]

570 allowed us to create an LC3B biosensor suitable for living cells. By following the FRET behavior of the

571 biosensor, we showed that the probe responds to the ATG4B-dependent changes in proLC3B priming. It was

572 previously reported that proLC3B is primed nearly instantaneously after translation, due to the constitutive

573 proteolytic activity of ATG4B [36,67]. In line with this, we found that the LC3B biosensor was almost

23

574 completely primed under basal conditions, without any detectable accumulation of proLC3B in cells. In

575 contrast, we showed that the proLC3B priming activity is altered in cells silenced for *ATG4B*, and that the

576 unprimed biosensor is located on or in close vicinity of puncta-shaped structures. Since the priming activity

577 of ATG4B is more efficient than its deconjugation activity, alterations in ATG4B levels were shown to mostly

578 affect deconjugation rather than priming [54]. Our findings using the LC3B biosensor were complementary

579 to this notion, as we were able to observe a stark increase in the number of Aqua-LC3B-II puncta structures

580 when *ATG4B* was silenced. By using a combination of broad and sensitive approaches to quantify FRET, we

581 provided the first proof of concept that proLC3B priming events occur at discrete sites in cells. It is likely that

582 these sites are already present to a lower extend under basal conditions, and they are highlighted only when

583 ATG4B priming activity is altered. With microscopy approaches with higher resolution, it might be possible

584 to reveal the existence of these reservoirs under basal conditions as well. In this light, the LC3B FRET

585 biosensor has the unique capacity to identify these priming reservoirs in living cells and with subcellular

586 resolution, underlining the superior sensitivity of the LC3B biosensor to explore the functional relevance of

587 these structures and the proteins regulating their formation. On the other hand, it should also be noted that the

588 biosensor is specific to ATG4B-LC3B axis, and it should not be intended as a generalized autophagy reporter.

589 Therefore, as with any other reporter, precaution should be taken when interpreting the results reported by the

590 biosensor and understand that the readouts are restricted to ATG4B/LC3B-mediated autophagy.

591 Furthermore, we confirmed that the isoform ATG4B is the major cysteine protease priming the LC3B

592 biosensor, and that its knockout results in a complete lack of priming. Additionally, we provided evidence that

593 ATG4A could mildly contribute to the priming of the LC3B biosensor in the absence of ATG4B, corroborating

594 previous findings concerning a functional redundancy among these isoforms [24,68]. Interestingly, our

595 biosensor provided novel information on the relevance of specific ATG4B residues for its priming activity. In

596 this light, we observed an unexpected ability of mutant ATG4B^{W142A} to fully prime proLC3B. Trp142 localizes

597 near the catalytic Cys74 residue, and it was suggested to be responsible for LC3 tail recognition [35]. In *in*

598 *vitro* cleavage assays, ATG4B with mutated Trp142 displayed a significantly reduced ability to cleave C-

599 terminally tagged LC3 [35]. Based on these findings, we were expecting to observe a reduced LC3B priming

600 with ATG4B^{W142A}, and no priming was expected with the catalytically-dead mutant ATG4B^{C74S}. While

601 ATG4B^{C74S} was incapable of priming proLC3B, we observed a full priming of the LC3B biosensor in the

602 presence of the ATG4B^{W142A} construct. Not only these results corroborate the high efficiency of ATG4B to

603 cleave proLC3B even in conditions where its catalytic activity is severely reduced, but they also highlight a

604 drastic difference between *in vitro* findings and data obtained in more complex paradigms.

605 Given the rising interest in developing inhibitors that block the early stages of autophagy by targeting

606 ATG4B, we challenged the LC3B biosensor with a selection of available inhibitors. Again, our biosensor

607 demonstrated to be a useful tool to investigate the mode of action and the efficacy of these compounds at the

608 concentrations and timepoints chosen for the analyses. First, we observed increased amounts of Aqua-LC3B-

609 II puncta after the incubation with all the inhibitors, indicating a reduction in the deconjugation activity of

610 ATG4B. These results were not surprising, as the deconjugation activity of ATG4B was reported to be less

611 efficient than the priming, and therefore more prone to get affected upon inhibition [54]. Furthermore, our

612 data also show that none of the inhibitors was able to completely abolish the priming activity of ATG4B

613 towards LC3B. Indeed, we did not observe a cytosolic distribution of the LC3B biosensor, nor ΔLifetime

614 values similar to those measured with the priming-defective G120A biosensor. Despite an incomplete

615 inhibition on priming, we found that the cells treated with NSC or ZPCK exhibited a significant reduction in

616 LC3B priming compared to control cells. Cells treated with MG132 – a proteasome inhibitor with a capacity

617 to inhibit cysteine proteases [55,56] – exhibited a significant increase in the mean ΔLifetime values, along

618 with a positive shift in the histogram mode value. In contrast, they did not display significant amounts of

619 pixels with high ΔLifetime. It is possible that the incubation with MG132 does not prevent the complete

620 degradation of tdLanYFP once this moiety has been cleaved from the biosensor. In this case, the presence of

621 tdLanYFP in the close vicinity of Aqua-LC3B-II puncta would lead to unspecific FRET events, potentially

622 unrelated to the proLC3B priming readout of the biosensor. This is the reason why a multi-parameter FRET

623 quantification – mean ΔLifetime, number of pixels with high ΔLifetime, histogram distribution of the

624 ΔLifetime values – is mandatory to characterize the specificity of ATG4B inhibitors. In this light, we propose

625 that an efficient ATG4B inhibitor should display a significant difference from controls in the three methods

626 of analysis. A compound that did not meet all the criteria but still displayed a significant increase in the number

627 of high-ΔLifetime pixels with a positive histogram mode value shift and showing a band compatible with the

628 unprimed biosensor was FMK-9a. Although FMK-based compounds were shown to be very potent ATG4B

629 inhibitors [30,50,69], a recent study showed that FMK-9a induces autophagy independently of its inhibition

630 on ATG4B activity [51]. Therefore, our findings support these results since FMK-9a did not meet all the

631 criteria to be considered as an efficient ATG4B inhibitor. Finally, our results on Tioconazole and LV-320

632 indicate that these two compounds inhibit the priming of proLC3B to a lesser extent than the other compounds.

633 Since they only displayed a positive shift in the histogram mode values and did not meet any other criteria,

634 we propose that they should be considered as mild ATG4B inhibitors. Overall, our results underline the lack

635 of inhibitors that can fully inhibit the priming activity of ATG4B. Future screenings using the LC3B biosensor

636 will be useful to identify new inhibitory compounds, as one would expect to observe a FRET behavior similar

637 to that of the G120A biosensor or *ATG4* KO cells in case of a full inhibition of proLC3B priming.

638 In addition to revealing the differential mode of actions of ATG4 inhibitors, the sensitivity of our

639 biosensor also allowed us to uncover a CDK1-dependent regulation of the ATG4B-LC3B axis at mitosis. Our

640 investigation in mitotic cells indicate that the inhibition of autophagy during cell division is not linked with

641 the accumulation of proLC3B reservoirs. However, the FRET response observed upon CDK1 inhibition in

642 mitotic cells suggests a CDK1-dependent regulation of ATG4B-LC3B nexus. We suggest that this regulation

643 could possibly be regulated by ULK1, one of the mitotic targets of CDK1 [63] . ULK1 is known to be activated

644 at the autophagosome formation site in interphase cells, where it phosphorylates ATG4B to inhibit its catalytic

645 activity towards LC3B [70]. Thus, CDK1 inhibition during mitosis could not only trigger the re-activation of

646 early autophagy targets such as ATG13, ULK1, ATG14 and TFEB [63], but it could also inactivate

647 downstream actors such as ATG4B and LC3B through the direct re-activation of ULK1 which, in turn, inhibits

648 ATG4B.

649 Since it is possible to calculate the number of pixels with high ΔLifetime, additional information can

650 be provided by localizing these pixels at the subcellular level. We observed a consistent presence of pixels

651 with high ΔLifetime around or on puncta-shaped structures, either upon ATG4B inhibition or *ATG4B*

652 silencing. In this light, we suggest that the local scarcity or the inhibition of ATG4B may cause alterations in

653 the proLC3B priming rates in discrete areas of the autophagosomes, which could be considered as priming

654 "hotspots". As previously mentioned, these reservoirs or "hotspots" with reduced proLC3B priming rates may

655 be sites where proLC3B is temporarily stored while trying to re-establish the full priming capacity of ATG4B.

656 Overall, we present the LC3B biosensor as a second-generation FRET biosensor that can report on the

657 regulation of the soluble and the lipidated forms of LC3B by ATG4B. First, this tool can be used to infer on

658 the structural properties of ATG4B and on its enzymatic activity. Thanks to its dual FRET/localization

659 readout, it can also be used to follow LC3B priming and turnover with superior spatiotemporal resolution.

660 Finally, the LC3B biosensor has the potential to be used in high-content screenings to identify more potent

661 ATG4B inhibitors and reveal their mode of action in living cells, which is a unique feature of the biosensor

662 compared to *in vitro* screening methodologies. Thus, the LC3B biosensor paves the way to ATG4B-targeted

663 therapies in complex diseases.

664 **Materials and Methods**

665 *Expression vectors and molecular cloning*

666 All the plasmids used in this study are listed in Supplementary Table 1. The cloning reactions were performed

667 using the Gibson Assembly Master Mix (New England Biolabs). Site-directed mutagenesis was performed

668 with the Quik-Change kit (Agilent). All the constructs from cloning and mutagenesis reactions were verified

669   using a 3130 XL sequencer (Applied Biosystems) and a BigDye Terminator V3.1 sequencing kit (Applied

670   Biosystems).

671

Cell culture and transfections

673   U2OS cells (HTB-96) were purchased from American Type Culture Collection. Control and *ATG4* KO HeLa

674   cells were kind gifts of Dr. Robin Ketteler (UCL, LMCB, United Kingdom). Cells were cultured in DMEM

675   (Thermo Fisher Scientific) supplemented with 10% FBS (Eurobio Scientific) and penicillin-streptomycin (100

676   U/mL, Thermo Fisher Scientific) and maintained at 37°C with 5% CO_2. All cell lines were routinely checked

677   for the absence of mycoplasma. Before imaging, normal growth media was replaced with phenol red-free

678   Leibovitz's L-15 medium (Thermo Fisher Scientific) supplemented with 20% FBS and penicillin-

679   streptomycin (100 U/mL). Cells were seeded at 70% confluence in Nunc Lab-Tek II Chamber slides (Thermo

680   Fisher Scientific) or Cellview cell culture slides (Greiner bio-one, 543979) for live cell imaging, 24-well plates

681   for immunocytochemistry, or 6-well plates for total cell lysates. Plasmid DNA transfection, or plasmid DNA

682   and siRNA co-transfection experiments were performed using Lipofectamine 2000 (Invitrogen) according to

683   the manufacturer's instructions. Cells were analyzed 48h after transfection. AllStars negative control siRNA

684   (SI03650318) and the *ATG4B*-specific siRNA (SI03156314) were purchased from QIAGEN.

685

Chemical compounds

687   The chemical compounds used in this study were as follows: Bafilomycin A1 (Sigma-Aldrich, B1793), FMK

688   9a (MedChemExpress, HY-100522), LV-320 (MedChemExpress, HY-112711), MG-132 (Selleckchem,

689   S2619), Nocodazole (Sigma-Aldrich, M1404), NSC 185058 (Selleckchem, S6716), RO-3306 (Sigma-

690   Aldrich, SML0569), Tioconazole (Sigma-Aldrich, 03907), Torin1 (Sigma-Aldrich, 475991), *Z-L*-Phe

691   chloromethyl ketone (Sigma-Aldrich, 860794). All chemical compounds were dissolved in dimethyl sulfoxide

692   (Sigma-Aldrich, D2438) and stored at -80°C. For starvation assay, a home-made Hank's Balanced Salt

693   Solution (HBSS) containing 8 mg/ml NaCl, 0.4 mg/ml KCl, 0.06 mg/ml KH_2PO_4, 0.048 mg/ml Na_2HPO_4

694   anhydrous, 1 mg/ml glucose, 0.348 mg/ml $NaHCO_3$ and penicillin-streptomycin (100 U/mL) was used.

695   Concentrations and durations of each treatment are indicated in the figure legends.

696

697   *Western blotting*

698   To collect total cell lysates, cells were rinsed with ice-cold Phosphate Buffer Saline (PBS) (Euromedex,

699   ET330-A) and lysed on ice in a buffer containing 50 mM Tris-HCL (pH 7.4), 150 mM NaCl, 1% Triton X-

700   100 (Euromedex, 2000-A), 1.5 mM $MgCl_2$, supplemented with 0.2 mM Na_3VO_4, 0.5 mM DTT (Thermo

701   Fisher Scientific, R0861), 4 mg/ml NaF, 5.4 mg/ml β-glycerolphosphate and a protease inhibitor cocktail

702   (Roche, 11873580001) immediately prior to lysis. Lysates were centrifuged at 13000 g for 20 minutes at 4°C.

703   Protein levels were quantified by using the Bradford protein assay dye reagent (BioRad, 5000006). Lysates

704   were then heated in Laemmli sample buffer at 95°C for 5 minutes, resolved in home-made Acrylamide/Bis

705   37.5:1 SDS-PAGE mini gels and transferred onto nitrocellulose membrane (Amersham™ Protran®,

706   10600004). Membranes were blocked in a solution containing 5% skimmed milk in TBS-T (TBS [Euromedex,

707   ET220] containing 0.1% Tween [Euromedex, 2001-B]) and incubated overnight at 4°C with primary

708   antibodies diluted in the blocking solution. The next day, membrane was washed in TBS-T, incubated with

709   the secondary antibody diluted in the blocking solution for 1h at room temperature, and washed again in TBS-

710   T prior to detection. The primary antibodies and dilutions were as follows: rabbit anti-Actin (Sigma-Aldrich,

711   A5060; 1:1000), ATG4B (Cell Signaling, 5299; 1:1000), LC3B (Cell Signaling, 3868; 1:1000). The secondary

712   antibody used was a horseradish-peroxidase-conjugated goat anti-rabbit antibody (Jackson ImmunoResearch;

713   1:6000-1:10000). After incubating the membrane in an ECL western blotting substrate (Thermo Fisher

714   Scientific, 32209), chemiluminescence signals were captured on a film (Thermo Fisher Scientific, 34091) and

715   developed with a CURIX 60 developer (Agfa Healthcare). The density of the bands was quantified by using

716   the *Gel Analyzer* function in Fiji (NIH) software. The relative abundance of each band was calculated by

717   normalizing the density of the band to that of the respective loading control.

718

Immunocytochemistry, confocal and FLIM microscopy

For immunocytochemistry, cells were seeded on 15 mm round coverslips placed onto 24-well plates. Cells were washed with 1X PBS and fixed in 1X PBS containing a mixture of 4% paraformaldehyde (Electron Microscopy Sciences, 15710) and 0.2% Glutaraldehyde (Euromedex, EM-16221) at room temperature for 20 minutes. After washing in 1X PBS, cells were permeabilized with 0.2% Triton in PBS for 10 minutes, washed again in 1X PBS and blocked for 1h in 5% BSA (Euromedex, 04-100-812-C) in 1X PBS at room temperature. Cells were incubated overnight at 4°C with primary antibodies diluted in the blocking buffer, and then washed with 1X PBS. Cells were then incubated with the secondary antibody diluted in the blocking buffer for 45 minutes at room temperature. Primary monoclonal anti-LAMP2 (Abcam, ab25631; 1:200) was used as a primary antibody and a goat anti-mouse IgG (H+L) cross-adsorbed antibody Alexa Fluor™ 647 (Thermo Fisher Scientific, A-21235; 1:500) was used as a secondary antibody. After washing in 1X PBS, coverslips were mounted in ProLong Gold Antifade reagent (Invitrogen, P36930). Cells were imaged with a Leica SP8 inverted confocal microscope equipped with a 63x oil immersion objective (NA 1.4). Aquamarine fluorescence was acquired with a 440 nm excitation laser, and an emission wavelength of 467-499 nm. The fluorescence of tdLanYFP and of LAMP2/Alexa 647 were captured by using a 514 nm and a 633 nm argon laser, respectively. The emission wavelengths were 525-565 nm for tdLanYFP, and 650-720 nm for LAMP2/Alexa 647. For FLIM analyses, images were acquired with a time-gated custom-made setup based on a spinning disk microscope as described in [71]. Aquamarine was used as a FRET donor in all experiments, and excited at 440 ± 10 nm with a supercontinuum picosecond pulsed laser source. Emission was selected using a band pass filter of 483/35 nm. The FLIM setup was controlled by the Inscoper Suite solution (Inscoper, France), and Aquamarine lifetime was measured in real-time during acquisition with the Inscoper software.

740

Image analysis

All the image analysis were performed in Fiji software. 3D puncta counting and fluorescence colocalization analyses illustrated in Fig. 1B-D and Fig. S1 were performed by using the macro developed by Cordelières and Zhang [72] in batch processing mode, and available in a GitHub repository at https://github.com/NEUBIAS/neubias-springer-book-2020. The minimum size of the objects for Aquamarine-LC3B and LAMP2/Alexa 647 was set to 10 voxels. The threshold to separate the objects from the background was set manually for both channels. The total number of objects in Aquamarine-LC3B channel was used to determine the number of Aqua-LC3B-II puncta-shaped structures. The objects in the Aquamarine-LC3B channel superposing with the LAMP2/Alexa 647 objects were used for colocalization analyses, and only the Aquamarine-LC3B objects superposing with the LAMP2/Alexa 647 objects with a ratio of 0.5 or more were quantified for analyses. The colocalizing objects were then normalized to the total number of Aquamarine-LC3B objects. For FLIM analysis, mean ΔLifetime values were calculated as previously described [38]. In all experiments, Aquamarine lifetime was calculated by the Inscoper software only when the pixel-by-pixel fluorescence intensity in the first gate was above 1000 grey levels. The number of Aqua-LC3B-II puncta structures in the accompanying fluorescence images (Fig. 2A, S2A, 5A-F, S9A-B) were quantified using the *Find Maxima* function in the Fiji imaging software, and by setting the prominence value as 1500. To analyze the high-ΔLifetime pixels, the *Histogram* tool in Fiji was used to measure the number of pixels with a lifetime between 2000 and 4000 psec. Each histogram was then converted to a ΔLifetime format by using the mean lifetime value of the donor-only construct as a normalizer. To determine the number of pixels with high ΔLifetime, the mean ΔLifetime value of the G120A biosensor or the mean ΔLifetime value of the WT biosensor expressed in *ATG4B* SKO cells were used as a threshold. The number of pixels showing G120A biosensor-like ΔLifetime or higher were then quantified and normalized to the total number of pixels, and this to determine the high-ΔLifetime pixel ratio per cell. For line analysis, a 17.8 µm linear region of interest (ROI) that contains both the high- and low-ΔLifetime pixels was manually drawn near or on the puncta-like structures. The *Plot profile* function in Fiji was then used to obtain ΔLifetime values on the drawn line, which

766 were then plotted. For histogram analyses, the average number of pixels per ΔLifetime was quantified for each

767 condition.

768

Statistical analysis

770 All statistical tests were performed by using GraphPad Prism 9. Two-way ANOVA with Tukey method was

771 applied to make multiple comparisons in the following figures: 1C-D; 2B-C, F; 3B-C; 4B-C; 5B-F; 6B-D; 7B-

772 C; S2B, F; S3B-C; S5A-B: S8B-C: S9B; S10B. Two-way ANOVA with two-stage step-up method of

773 Benjamini, Krieger and Yekutieli was applied to make multiple comparisons in the following figures: 1F-G,

774 S2D and S5D. Correlation analysis between the ΔLifetime values and the puncta numbers were performed to

775 compute R^2 and P values in Fig. S6.

776

Figure preparation

778 The cartoon in Figure 1A was prepared by using the illustrations available at https://smart.servier.com/ [73].

779 Graphs and figures were assembled in GraphPad Prism 9 and Inkscape, respectively.

780

Data and material availability

782 Plasmids and macro used in this study and the source data that support the findings are available from the

783 corresponding authors (G.B. [giulia.bertolin@univ-rennes1.fr] and M.T. [marc.tramier@univ-rennes1.fr]) on

784 request.

785

Acknowledgments

799

Author Contributions

801   E.B.G. designed, performed and analyzed the experiments and wrote the manuscript; A.C. performed the

802   experiments and revised the manuscript, M.T. co-supervised the work, revised the manuscript and provided

803   funding; G.B. co-supervised the work, designed the experiments, edited and revised the manuscript, and

804   provided funding.

805

Conflict of interest

807   The authors declare no conflict of interest.

808

References

810   1.   Ohsumi, Y. Historical Landmarks of Autophagy Research. *Cell Research* **2014**, *24*, 9–23, doi:10.1038/cr.2013.169.

811   2.   Klionsky, D.J.; Emr, S.D. Autophagy as a Regulated Pathway of Cellular Degradation. *Science* **2000**, *290*, 1717–1721,
812   doi:10.1126/science.290.5497.1717.

813   3.   Deretic, V.; Levine, B. Autophagy, Immunity, and Microbial Adaptations. *Cell Host & Microbe* **2009**, *5*, 527–549,
814   doi:10.1016/j.chom.2009.05.016.

815   4.   Rodriguez-Rocha, H.; Garcia-Garcia, A.; Panayiotidis, M.I.; Franco, R. DNA Damage and Autophagy. *Mutation Research/Fundamental*
816   *and Molecular Mechanisms of Mutagenesis* **2011**, *711*, 158–166, doi:10.1016/j.mrfmmm.2011.03.007.

817   5.   Axe, E.L.; Walker, S.A.; Manifava, M.; Chandra, P.; Roderick, H.L.; Habermann, A.; Griffiths, G.; Ktistakis, N.T. Autophagosome
818   Formation from Membrane Compartments Enriched in Phosphatidylinositol 3-Phosphate and Dynamically Connected to the Endoplasmic
819   Reticulum. *J Cell Biol* **2008**, *182*, 685–701, doi:10.1083/jcb.200803137.

820   6.   Mizushima, N.; Yoshimori, T.; Ohsumi, Y. The Role of Atg Proteins in Autophagosome Formation. *Annu Rev Cell Dev Biol* **2011**, *27*,
821   107–132, doi:10.1146/annurev-cellbio-092910-154005.

7. Ichimura, Y.; Kirisako, T.; Takao, T.; Satomi, Y.; Shimonishi, Y.; Ishihara, N.; Mizushima, N.; Tanida, I.; Kominami, E.; Ohsumi, M.; et al. A Ubiquitin-like System Mediates Protein Lipidation. *Nature* **2000**, *408*, 488–492, doi:10.1038/35044114.

8. Weidberg, H.; Shvets, E.; Shpilka, T.; Shimron, F.; Shinder, V.; Elazar, Z. LC3 and GATE-16/GABARAP Subfamilies Are Both Essential yet Act Differently in Autophagosome Biogenesis. *The EMBO Journal* **2010**, *29*, 1792–1802, doi:10.1038/emboj.2010.74.

9. Noda, N.N.; Ohsumi, Y.; Inagaki, F. Atg8-Family Interacting Motif Crucial for Selective Autophagy. *FEBS Letters* **2010**, *584*, 1379–1385, doi:10.1016/j.febslet.2010.01.018.

10. Shpilka, T.; Weidberg, H.; Pietrokovski, S.; Elazar, Z. Atg8: An Autophagy-Related Ubiquitin-like Protein Family. *Genome Biology* **2011**, *12*, 226, doi:10.1186/gb-2011-12-7-226.

11. Jatana, N.; Ascher, D.B.; Pires, D.E.V.; Gokhale, R.S.; Thukral, L. Human LC3 and GABARAP Subfamily Members Achieve Functional Specificity via Specific Structural Modulations. *Autophagy* **2020**, *16*, 239–255, doi:10.1080/15548627.2019.1606636.

12. Kirisako, T.; Ichimura, Y.; Okada, H.; Kabeya, Y.; Mizushima, N.; Yoshimori, T.; Ohsumi, M.; Takao, T.; Noda, T.; Ohsumi, Y. The Reversible Modification Regulates the Membrane-Binding State of Apg8/Aut7 Essential for Autophagy and the Cytoplasm to Vacuole Targeting Pathway. *J Cell Biol* **2000**, *151*, 263–276, doi:10.1083/jcb.151.2.263.

13. Tanida, I.; Sou, Y.; Ezaki, J.; Minematsu-Ikeguchi, N.; Ueno, T.; Kominami, E. HsAtg4B/HsApg4B/Autophagin-1 Cleaves the Carboxyl Termini of Three Human Atg8 Homologues and Delipidates Microtubule-Associated Protein Light Chain 3- and GABAA Receptor-Associated Protein-Phospholipid Conjugates. *J Biol Chem* **2004**, *279*, 36268–36276, doi:10.1074/jbc.M401461200.

14. Kabeya, Y.; Mizushima, N.; Yamamoto, A.; Oshitani-Okamoto, S.; Ohsumi, Y.; Yoshimori, T. LC3, GABARAP and GATE16 Localize to Autophagosomal Membrane Depending on Form-II Formation. *Journal of Cell Science* **2004**, *117*, 2805–2812, doi:10.1242/jcs.01131.

15. Hanada, T.; Noda, N.N.; Satomi, Y.; Ichimura, Y.; Fujioka, Y.; Takao, T.; Inagaki, F.; Ohsumi, Y. The Atg12-Atg5 Conjugate Has a Novel E3-like Activity for Protein Lipidation in Autophagy. *J Biol Chem* **2007**, *282*, 37298–37302, doi:10.1074/jbc.C700195200.

16. Martens, S.; Fracchiolla, D. Activation and Targeting of ATG8 Protein Lipidation. *Cell Discov* **2020**, *6*, 1–11, doi:10.1038/s41421-020-0155-1.

17. Nakatogawa, H.; Ichimura, Y.; Ohsumi, Y. Atg8, a Ubiquitin-like Protein Required for Autophagosome Formation, Mediates Membrane Tethering and Hemifusion. *Cell* **2007**, *130*, 165–178, doi:10.1016/j.cell.2007.05.021.

18. Xie, Z.; Nair, U.; Klionsky, D.J. Atg8 Controls Phagophore Expansion during Autophagosome Formation. *Mol Biol Cell* **2008**, *19*, 3290–3298, doi:10.1091/mbc.E07-12-1292.

19. Pankiv, S.; Clausen, T.H.; Lamark, T.; Brech, A.; Bruun, J.-A.; Outzen, H.; Øvervatn, A.; Bjørkøy, G.; Johansen, T. P62/SQSTM1 Binds Directly to Atg8/LC3 to Facilitate Degradation of Ubiquitinated Protein Aggregates by Autophagy. *J Biol Chem* **2007**, *282*, 24131–24145, doi:10.1074/jbc.M702824200.

20. Mizushima, N. The ATG Conjugation Systems in Autophagy. *Current Opinion in Cell Biology* **2020**, *63*, 1–10, doi:10.1016/j.ceb.2019.12.001.

21. Nair, U.; Yen, W.-L.; Mari, M.; Cao, Y.; Xie, Z.; Baba, M.; Reggiori, F.; Klionsky, D.J. A Role for Atg8–PE Deconjugation in Autophagosome Biogenesis. *Autophagy* **2012**, *8*, 780–793, doi:10.4161/auto.19385.

22. Nakatogawa, H.; Ishii, J.; Asai, E.; Ohsumi, Y. Atg4 Recycles Inappropriately Lipidated Atg8 to Promote Autophagosome Biogenesis. *Autophagy* **2012**, *8*, 177–186, doi:10.4161/auto.8.2.18373.

23. Yu, Z.-Q.; Ni, T.; Hong, B.; Wang, H.-Y.; Jiang, F.-J.; Zou, S.; Chen, Y.; Zheng, X.-L.; Klionsky, D.J.; Liang, Y.; et al. Dual Roles of Atg8−PE Deconjugation by Atg4 in Autophagy. *Autophagy* **2012**, *8*, 883–892, doi:10.4161/auto.19652.

24. Agrotis, A.; Pengo, N.; Burden, J.J.; Ketteler, R. Redundancy of Human ATG4 Protease Isoforms in Autophagy and LC3/GABARAP Processing Revealed in Cells. *Autophagy* **2019**, *15*, 976–997, doi:10.1080/15548627.2019.1569925.

25. Nguyen, T.N.; Padman, B.S.; Zellner, S.; Khuu, G.; Uoselis, L.; Lam, W.K.; Skulsuppaisarn, M.; Lindblom, R.S.J.; Watts, E.M.; Behrends, C.; et al. ATG4 Family Proteins Drive Phagophore Growth Independently of the LC3/GABARAP Lipidation System. *Mol Cell* **2021**, *81*, 2013-2030.e9, doi:10.1016/j.molcel.2021.03.001.

26. Betin, V.M.S.; Singleton, B.K.; Parsons, S.F.; Anstee, D.J.; Lane, J.D. Autophagy Facilitates Organelle Clearance during Differentiation of Human Erythroblasts: Evidence for a Role for ATG4 Paralogs during Autophagosome Maturation. *Autophagy* **2013**, *9*, 881–893, doi:10.4161/auto.24172.

27. Levine, B.; Kroemer, G. Biological Functions of Autophagy Genes: A Disease Perspective. *Cell* **2019**, *176*, 11–42, doi:10.1016/j.cell.2018.09.048.

28. Galluzzi, L.; Bravo-San Pedro, J.M.; Levine, B.; Green, D.R.; Kroemer, G. Pharmacological Modulation of Autophagy: Therapeutic Potential and Persisting Obstacles. *Nature Reviews Drug Discovery* **2017**, *16*, 487–511, doi:10.1038/nrd.2017.22.

29. Ariosa, A.R.; Lahiri, V.; Lei, Y.; Yang, Y.; Yin, Z.; Zhang, Z.; Klionsky, D.J. A Perspective on the Role of Autophagy in Cancer. *Biochimica et Biophysica Acta (BBA) - Molecular Basis of Disease* **2021**, *1867*, 166262, doi:10.1016/j.bbadis.2021.166262.

30. Agrotis, A.; Ketteler, R. On ATG4B as Drug Target for Treatment of Solid Tumours-The Knowns and the Unknowns. *Cells* **2019**, *9*, E53, doi:10.3390/cells9010053.

31. *Principles of Fluorescence Spectroscopy*;

32. Truong, K.; Ikura, M. The Use of FRET Imaging Microscopy to Detect Protein–Protein Interactions and Protein Conformational Changes in Vivo. *Current Opinion in Structural Biology* **2001**, *11*, 573–578, doi:10.1016/S0959-440X(00)00249-9.

33. Sizaire, F.; Tramier, M. FRET-Based Biosensors: Genetically Encoded Tools to Track Kinase Activity in Living Cells. *Protein Phosphorylation* **2017**, doi:10.5772/intechopen.71005.

34. Padilla-Parra, S.; Tramier, M. FRET Microscopy in the Living Cell: Different Approaches, Strengths and Weaknesses. *Truong & Ikura* **2012**, *34*, 369–376, doi:10.1002/bies.201100086.

35. Sugawara, K.; Suzuki, N.N.; Fujioka, Y.; Mizushima, N.; Ohsumi, Y.; Inagaki, F. Structural Basis for the Specificity and Catalysis of Human Atg4B Responsible for Mammalian Autophagy. *J Biol Chem* **2005**, *280*, 40058–40065, doi:10.1074/jbc.M509158200.

36. Kabeya, Y.; Mizushima, N.; Ueno, T.; Yamamoto, A.; Kirisako, T.; Noda, T.; Kominami, E.; Ohsumi, Y.; Yoshimori, T. LC3, a Mammalian Homologue of Yeast Apg8p, Is Localized in Autophagosome Membranes after Processing. *EMBO J* **2000**, *19*, 5720–5728, doi:10.1093/emboj/19.21.5720.

37. Erard, M.; Fredj, A.; Pasquier, H.; Beltolngar, D.-B.; Bousmah, Y.; Derrien, V.; Vincent, P.; Merola, F. Minimum Set of Mutations Needed to Optimize Cyan Fluorescent Proteins for Live Cell Imaging. *Mol. BioSyst.* **2013**, *9*, 258–267, doi:10.1039/C2MB25303H.

38. Bertolin, G.; Sizaire, F.; Déméautis, C.; Chapuis, C.; Mérola, F.; Erard, M.; Tramier, M. Optimized FRET Pairs and Quantification Approaches To Detect the Activation of Aurora Kinase A at Mitosis. *ACS Sens* **2019**, *4*, 2018–2027, doi:10.1021/acssensors.9b00486.

39. Bousmah, Y.; Valenta, H.; Bertolin, G.; Singh, U.; Nicolas, V.; Pasquier, H.; Tramier, M.; Merola, F.; Erard, M. TdLanYFP, a Yellow, Bright, Photostable, and PH-Insensitive Fluorescent Protein for Live-Cell Imaging and Förster Resonance Energy Transfer-Based Sensing Strategies. *ACS Sens* **2021**, *6*, 3940–3947, doi:10.1021/acssensors.1c00874.

40. Tanida, I.; Minematsu-Ikeguchi, N.; Ueno, T.; Kominami, E. Lysosomal Turnover, but Not a Cellular Level, of Endogenous LC3 Is a Marker for Autophagy. *Autophagy* **2005**, *1*, 84–91, doi:10.4161/auto.1.2.1697.

41. Nash, Y.; Schmukler, E.; Trudler, D.; Pinkas-Kramarski, R.; Frenkel, D. DJ-1 Deficiency Impairs Autophagy and Reduces Alpha-Synuclein Phagocytosis by Microglia. *J Neurochem* **2017**, *143*, 584–594, doi:10.1111/jnc.14222.

42. Li, M.; Hou, Y.; Wang, J.; Chen, X.; Shao, Z.-M.; Yin, X.-M. Kinetics Comparisons of Mammalian Atg4 Homologues Indicate Selective Preferences toward Diverse Atg8 Substrates. *J Biol Chem* **2011**, *286*, 7327–7338, doi:10.1074/jbc.M110.199059.

43. Agrotis, A.; von Chamier, L.; Oliver, H.; Kiso, K.; Singh, T.; Ketteler, R. Human ATG4 Autophagy Proteases Counteract Attachment of Ubiquitin-like LC3/GABARAP Proteins to Other Cellular Proteins. *Journal of Biological Chemistry* **2019**, *294*, 12610–12621, doi:10.1074/jbc.AC119.009977.

44. Wang, W.; Chen, Z.; Billiar, T.R.; Stang, M.T.; Gao, W. The Carboxyl-Terminal Amino Acids Render Pro-Human LC3B Migration Similar to Lipidated LC3B in SDS-PAGE. *PLOS ONE* **2013**, *8*, e74222, doi:10.1371/journal.pone.0074222.

45. Li, M. Kinetics Comparisons of Mammalian Atg4 Homologues Indicate Selective Preferences toward Diverse Atg8 Substrates*. **2011**, *286*, 12.

46. Fujita, N.; Hayashi-Nishino, M.; Fukumoto, H.; Omori, H.; Yamamoto, A.; Noda, T.; Yoshimori, T. An Atg4B Mutant Hampers the Lipidation of LC3 Paralogues and Causes Defects in Autophagosome Closure. *Mol Biol Cell* **2008**, *19*, 4651–4659, doi:10.1091/mbc.e08-03-0312.

47. Skytte Rasmussen, M.; Mouilleron, S.; Kumar Shrestha, B.; Wirth, M.; Lee, R.; Bowitz Larsen, K.; Abudu Princely, Y.; O'Reilly, N.; Sjøttem, E.; Tooze, S.A.; et al. ATG4B Contains a C-Terminal LIR Motif Important for Binding and Efficient Cleavage of Mammalian Orthologs of Yeast Atg8. *Autophagy* **2017**, *13*, 834–853, doi:10.1080/15548627.2017.1287651.

48. Liu, P.-F.; Tsai, K.-L.; Hsu, C.-J.; Tsai, W.-L.; Cheng, J.-S.; Chang, H.-W.; Shiau, C.-W.; Goan, Y.-G.; Tseng, H.-H.; Wu, C.-H.; et al. Drug Repurposing Screening Identifies Tioconazole as an ATG4 Inhibitor That Suppresses Autophagy and Sensitizes Cancer Cells to Chemotherapy. *Theranostics* **2018**, *8*, 830–845, doi:10.7150/thno.22012.

49. Bosc, D.; Vezenkov, L.; Bortnik, S.; An, J.; Xu, J.; Choutka, C.; Hannigan, A.M.; Kovacic, S.; Loo, S.; Clark, P.G.K.; et al. A New Quinoline-Based Chemical Probe Inhibits the Autophagy-Related Cysteine Protease ATG4B. *Sci Rep* **2018**, *8*, 11653, doi:10.1038/s41598-018-29900-x.

50. Qiu, Z.; Kuhn, B.; Aebi, J.; Lin, X.; Ding, H.; Zhou, Z.; Xu, Z.; Xu, D.; Han, L.; Liu, C.; et al. Discovery of Fluoromethylketone-Based Peptidomimetics as Covalent ATG4B (Autophagin-1) Inhibitors Available online: https://pubs.acs.org/doi/pdf/10.1021/acsmedchemlett.6b00208 (accessed on 5 April 2022).

51. Chu, J.; Fu, Y.; Xu, J.; Zheng, X.; Gu, Q.; Luo, X.; Dai, Q.; Zhang, S.; Liu, P.; Hong, L.; et al. ATG4B Inhibitor FMK-9a Induces Autophagy Independent on Its Enzyme Inhibition. *Arch Biochem Biophys* **2018**, *644*, 29–36, doi:10.1016/j.abb.2018.03.001.

52. Akin, D.; Wang, S.K.; Habibzadegah-Tari, P.; Law, B.; Ostrov, D.; Li, M.; Yin, X.-M.; Kim, J.-S.; Horenstein, N.; Dunn, W.A. A Novel ATG4B Antagonist Inhibits Autophagy and Has a Negative Impact on Osteosarcoma Tumors. *Autophagy* **2014**, *10*, 2021–2035, doi:10.4161/auto.32229.

53. Nguyen, T.G.; Honson, N.S.; Arns, S.; Davis, T.L.; Dhe-Paganon, S.; Kovacic, S.; Kumar, N.S.; Pfeifer, T.A.; Young, R.N. Development of Fluorescent Substrates and Assays for the Key Autophagy-Related Cysteine Protease Enzyme, ATG4B. *Assay Drug Dev Technol* **2014**, *12*, 176–189, doi:10.1089/adt.2013.561.

54. Kauffman, K.J.; Yu, S.; Jin, J.; Mugo, B.; Nguyen, N.; O'Brien, A.; Nag, S.; Lystad, A.H.; Melia, T.J. Delipidation of Mammalian Atg8-Family Proteins by Each of the Four ATG4 Proteases. *Autophagy* **2018**, *14*, 992–1010, doi:10.1080/15548627.2018.1437341.

55. Steinhilb, M.L.; Turner, R.S.; Gaut, J.R. The Protease Inhibitor, MG132, Blocks Maturation of the Amyloid Precursor Protein Swedish Mutant Preventing Cleavage by Beta-Secretase. *J Biol Chem* **2001**, *276*, 4476–4484, doi:10.1074/jbc.M008793200.

56. Harer, S.L.; Bhatia, M.S.; Bhatia, N.M. Proteasome Inhibitors Mechanism; Source for Design of Newer Therapeutic Agents. *J Antibiot* **2012**, *65*, 279–288, doi:10.1038/ja.2011.84.

57. Eskelinen, E.-L.; Prescott, A.R.; Cooper, J.; Brachmann, S.M.; Wang, L.; Tang, X.; Backer, J.M.; Lucocq, J.M. Inhibition of Autophagy in Mitotic Animal Cells. *Traffic* **2002**, *3*, 878–893, doi:10.1034/j.1600-0854.2002.31204.x.

58. Furuya, T.; Kim, M.; Lipinski, M.; Li, J.; Kim, D.; Lu, T.; Shen, Y.; Rameh, L.; Yankner, B.; Tsai, L.-H.; et al. Negative Regulation of Vps34 by Cdk Mediated Phosphorylation. *Mol Cell* **2010**, *38*, 500–511, doi:10.1016/j.molcel.2010.05.009.

59. Mathiassen, S.G.; De Zio, D.; Cecconi, F. Autophagy and the Cell Cycle: A Complex Landscape. *Front Oncol* **2017**, *7*, 51, doi:10.3389/fonc.2017.00051.

60. Li, Z.; Ji, X.; Wang, D.; Liu, J.; Zhang, X. Autophagic Flux Is Highly Active in Early Mitosis and Differentially Regulated throughout the Cell Cycle. *Oncotarget* **2016**, *7*, 39705–39718, doi:10.18632/oncotarget.9451.

61. Loukil, A.; Zonca, M.; Rebouissou, C.; Baldin, V.; Coux, O.; Biard-Piechaczyk, M.; Blanchard, J.-M.; Peter, M. High-Resolution Live-Cell Imaging Reveals Novel Cyclin A2 Degradation Foci Involving Autophagy. *J Cell Sci* **2014**, *127*, 2145–2150, doi:10.1242/jcs.139188.

62. Liu, L.; Xie, R.; Nguyen, S.; Ye, M.; McKeehan, W.L. Robust Autophagy/Mitophagy Persists during Mitosis. *Cell Cycle* **2009**, *8*, 1616–1620, doi:10.4161/cc.8.10.8577.

63. Odle, R.I.; Walker, S.A.; Oxley, D.; Kidger, A.M.; Balmanno, K.; Gilley, R.; Okkenhaug, H.; Florey, O.; Ktistakis, N.T.; Cook, S.J. An MTORC1-to-CDK1 Switch Maintains Autophagy Suppression during Mitosis. *Mol Cell* **2020**, *77*, 228-240.e7, doi:10.1016/j.molcel.2019.10.016.

64. Horn, R.D.V.; Chu, S.; Fan, L.; Yin, T.; Du, J.; Beckmann, R.; Mader, M.; Zhu, G.; Toth, J.; Blanchard, K.; et al. Cdk1 Activity Is Required for Mitotic Activation of Aurora A during G2/M Transition of Human Cells. *Journal of Biological Chemistry* **2010**, *285*, 21849–21857, doi:10.1074/jbc.M110.141010.

954 65. Klionsky, D.J.; Abdel-Aziz, A.K.; Abdelfatah, S.; Abdellatif, M.; Abdoli, A.; Abel, S.; Abeliovich, H.; Abildgaard, M.H.; Abudu, Y.P.;
955   Acevedo-Arozena, A.; et al. Guidelines for the Use and Interpretation of Assays for Monitoring Autophagy (4th Edition). *null* **2021**, 1–382,
956   doi:10.1080/15548627.2020.1797280.
957 66. Li, M.; Chen, X.; Ye, Q.-Z.; Vogt, A.; Yin, X.-M. A High-Throughput FRET-Based Assay for Determination of Atg4 Activity. *Autophagy*
958   **2012**, *8*, 401–412, doi:10.4161/auto.18777.
959 67. Scherz-Shouval, R.; Shvets, E.; Fass, E.; Shorer, H.; Gil, L.; Elazar, Z. Reactive Oxygen Species Are Essential for Autophagy and
960   Specifically Regulate the Activity of Atg4. *EMBO J* **2007**, *26*, 1749–1760, doi:10.1038/sj.emboj.7601623.
961 68. Nguyen, N.; Olivas, T.J.; Mires, A.; Jin, J.; Yu, S.; Luan, L.; Nag, S.; Kauffman, K.J.; Melia, T.J. The Insufficiency of ATG4A in
962   Macroautophagy. *Journal of Biological Chemistry* **2020**, *295*, 13584–13600, doi:10.1074/jbc.RA120.013897.
963 69. Xu, D.; Xu, Z.; Han, L.; Liu, C.; Zhou, Z.; Qiu, Z.; Lin, X.; Tang, G.; Shen, H.; Aebi, J.; et al. Identification of New ATG4B Inhibitors
964   Based on a Novel High-Throughput Screening Platform. *SLAS Discov* **2017**, *22*, 338–347, doi:10.1177/1087057116639202.
965 70. Pengo, N.; Agrotis, A.; Prak, K.; Jones, J.; Ketteler, R. A Reversible Phospho-Switch Mediated by ULK1 Regulates the Activity of
966   Autophagy Protease ATG4B. *Nat Commun* **2017**, *8*, 294, doi:10.1038/s41467-017-00303-2.
967 71. Bertolin, G.; Sizaire, F.; Herbomel, G.; Reboutier, D.; Prigent, C.; Tramier, M. A FRET Biosensor Reveals Spatiotemporal Activation and
968   Functions of Aurora Kinase A in Living Cells. *Nat Commun* **2016**, *7*, 12674, doi:10.1038/ncomms12674.
969 72. Cordelières, F.P.; Zhang, C. 3D Quantitative Colocalisation Analysis. In *Bioimage Data Analysis Workflows*; Miura, K., Sladoje, N., Eds.;
970   Learning Materials in Biosciences; Springer International Publishing: Cham, 2020; pp. 33–66 ISBN 978-3-030-22386-1.
971 73. SMART Available online: https://smart.servier.com/ (accessed on 3 May 2022).
972
973

The LC3B FRET biosensor monitors the modes of action of ATG4B during autophagy in living cells

Elif Begüm Gökerküçük et al.

Main figures

Figure 1. The LC3B biosensor reports on autophagy induction and/or lysosomal inhibition, and colocalizes with LAMP2 in an autophagy-dependent manner. (**A**) The cartoon illustrates the design and the mode of action of the LC3B biosensor. The biosensor was designed to flank the N- and C- termini of proLC3B with a donor (D, Aquamarine)-acceptor (A, tdLanYFP) FRET pair. When ATG4 is not active, the biosensor is expected to remain unprocessed in cells, allowing Aquamarine and tdLanYFP to perform FRET. Upon the proteolytic activity of ATG4, the biosensor is expected to be cleaved at its C-terminus, in turn losing its tdLanYFP moiety and the FRET effect with it. A successful priming of the biosensor is expected to yield Aquamarine-LC3B-I, which can then be integrated into the PE head groups of the phagophores and observed as puncta-shaped structures. The resulting Aquamarine-LC3B-II puncta-shaped structures can then be quantified to estimate the number of autophagosomes. (**B**) Representative fluorescence images of U2OS cells expressing the WT biosensor and stained for endogenous LAMP2. To investigate the changes in Aqua-LC3B puncta numbers and their colocalization with LAMP2, cells were treated with the following compounds: DMSO (6h), BafA$_1$ (6h, 100 nM), Torin1 (3h, 250 nM), Torin1 (3h, 250 nM) + BafA$_1$ (6h, 100 nM), HBSS (1h), HBSS (1h) + BafA1 (6h, 100 nM). Scale bar: 9 µm. (**C**) Quantification of the number of Aqua-LC3B-II puncta in cells expressing the WT or G120A biosensor and treated as indicated. (**D**) Quantification of the ratio of Aqua-LC3B-II puncta structures colocalizing with LAMP2-positive objects in cells expressing the WT or G120A biosensor and treated as indicated. n = 10 cells per condition from one representative experiment (of three) in (**C**) and (**D**). (**E**) Representative western blotting images and corresponding quantifications (**F, G**) of total lysates from U2OS cells expressing the WT or G120A biosensor and treated as indicated. IB1 and IB2 correspond to the same lysates blotted for overexpressed (IB1) or endogenous (IB2) LC3B forms. Loading control: Actin. n = 3 independent experiments *P < 0.05, **P < 0.01, ***P < 0.001, ****P < 0.0001, ns (not significant) as determined by two-way ANOVA with Tukey's multiple comparison test in (**C**) and (**D**), and with two-stage step-up method of Benjamini, Krieger and Yekutieli's multiple comparison test to control the false discovery rate in (**F**) and (**G**).

Figure 2. The knockdown of *ATG4B* lowers the priming of the LC3B biosensor. (**A**) Representative fluorescence and ΔLifetime images of U2OS cells co-expressing the WT or G120A biosensor with control or *ATG4B*-specific siRNAs, and analyzed by FRET/FLIM. Squares on the top images of WT or G120A biosensor panels illustrate the location of the enlarged images. Dotted lines on the enlarged images illustrate where the line analysis was performed. Pseudocolor scale: pixel-by-pixel ΔLifetime. Scale bars: overviews, 40 μm; enlarged, 6 μm. Mean ΔLifetime (**B**), number of high ΔLifetime pixels (**C**), line (**D**), histogram (**E**), and number of Aqua-LC3B-II puncta (**F**) analyses of U2OS cells co-expressing the WT or G120A biosensor with control or *ATG4B*-specific siRNAs in (**B**), (**D**), (**E**) and (**F**), and the WT donor or biosensor with control or *ATG4B* siRNA in (**C**). Vertical dotted lines on each histogram depicts the mode value in (**E**). $n = 10$ cells per condition from one representative experiment (of three) in (**B**), (**C**), (**E**) and (**F**). $**P < 0.01$, $****P < 0.0001$, ns (not significant) as determined by two-way ANOVA with Tukey's multiple comparison test in (**B**), (**C**) and (**F**).

**Figure 3.** The absence of ATG4B maximizes the FRET response of the LC3B biosensor. (**A**) Representative fluorescence and ΔLifetime images of HeLa control, *ATG4B* SKO, *ATG4A/B* DKO, *ATG4A/B/C* TKO cells expressing the WT or G120A biosensor and analyzed by FRET/FLIM. Pseudocolor scale: pixel-by-pixel ΔLifetime. Scale bar: 40 μm. Mean ΔLifetime (**B**), number of high ΔLifetime pixels (**C**) and histogram (**D**) analyses of HeLa control, *ATG4B* SKO, *ATG4A/B* DKO, *ATG4A/B/C* TKO cells expressing the WT or G120A biosensor. The vertical dotted lines on each histogram depict the mode value in (**D**). *n* = 10 cells per condition from one representative experiment (of three) in (**B**), (**C**) and (**D**). **P < 0.01, ****P < 0.0001, ns (not significant) as determined by two-way ANOVA with Tukey's multiple comparison test in (**B**) and (**C**).

Figure 4. The priming deficiency of the LC3B biosensor is rescued when expressing WT or ATG4B^{W142A} in *ATG4B* SKO cells. (**A**) Representative fluorescence and ΔLifetime images of control and *ATG4B* SKO HeLa cells co-expressing the WT biosensor with an empty vector, or with vectors expressing WT ATG4B, ATG4B^{C74S} or ATG4B^{W142A}, and analyzed by FRET/FLIM. Pseudocolor scale: pixel-by-pixel ΔLifetime. Scale bar: 40 μm. Mean ΔLifetime (**B**) and number of high ΔLifetime pixels (**C**) analyses of control and *ATG4B* SKO cells co-expressing the WT biosensor with an empty vector, or with vectors expressing WT ATG4B, ATG4B^{C74S} or ATG4B^{W142A}. (**D**) The histogram analysis of *ATG4B* SKO cells co-expressing the WT biosensor with an empty vector, or with vectors expressing WT ATG4B, ATG4B^{C74S} or ATG4B^{W142A}. Vertical dotted lines on each histogram depict the mode value in (**D**). $n = 10$ cells per condition from one representative experiment (of three) in (**B**), (**C**) and (**D**). ****$P < 0.0001$, ns (not significant) as determined by two-way ANOVA with Tukey's multiple comparison test in (**B**) and (**C**).

Figure 5. ATG4B inhibitors variably alter the ΔLifetime behavior and LC3B puncta number in cells expressing the LC3B biosensor. (**A**) Representative fluorescence and ΔLifetime images of HeLa cells expressing the WT or G120A biosensor, treated with DMSO (6h), and analyzed by FRET/FLIM. Representative fluorescence and ΔLifetime images of HeLa cells expressing the WT biosensor and treated with Tioconazole (6h, 4 μM) (**B**), LV-320 (6h, 120 μM) (**C**), FMK-9a (6h, 10 μM) (**D**), NSC 185058 (6h, 100 μM) (**E**), or *Z-L*-Phe chloromethyl ketone (6h, 3 μM) (**F**). Mean ΔLifetime and number of Aqua-LC3B-II puncta analyses of HeLa cells expressing the WT or G120A biosensor and treated with Tioconazole (6h, 4μM) (**B**), LV-320 (6h, 120 μM) (**C**), FMK-9a (6h, 10 μM) (**D**), NSC 185058 (6h, 100 μM) (**E**), or *Z-L*-Phe chloromethyl ketone (6h, 3 μM) (**F**). Pseudocolor scale: pixel-by-pixel ΔLifetime. Scale bars: 40 μm. *n* = 10 cells per condition from one representative experiment (of three) in (**B-F**). *$P < 0.05$, **$P < 0.01$, ***$P < 0.001$, ****$P < 0.0001$, ns (not significant) as determined by two-way ANOVA with Tukey's multiple comparison test in (**B-F**).

**Figure 6.** The LC3B biosensor reveals the mode of action of FMK-9a, NSC 185058 and *Z-L*-Phe chloromethyl ketone in cells. (**A**) Representative fluorescence and ΔLifetime images of HeLa cells expressing the WT or G120A biosensor, treated with DMSO (6h), and analyzed by FRET/FLIM. Representative fluorescence and ΔLifetime images of HeLa cells expressing the WT biosensor and treated with the following compounds: FMK-9a (6h, 10 μM) (**B**), NSC 185058 (6h, 100 μM) (**C**), or *Z-L*-Phe chloromethyl ketone (6h, 3 μM) (**D**). Squares on the top images of WT or G120A biosensor panels illustrate the location of the enlarged images. Dotted lines on the enlarged images illustrate where the line analysis was performed. Pseudocolor scale: pixel-by-pixel ΔLifetime. Scale bars: overviews, 40 μm; enlarged, 6 μm. Number of high ΔLifetime pixels analysis of HeLa cells expressing the WT donor or biosensor and treated with FMK-9a (6h, 10 μM) (**B**), NSC 185058 (6h, 100 μM) (**C**), or *Z-L*-Phe chloromethyl ketone (6h, 3 μM) (**D**). Line and histogram analyses of HeLa cells expressing the WT or G120A biosensor and treated with FMK-9a (6h, 10 μM) (**B**), NSC 185058 (6h, 100 μM) (**C**), or *Z-L*-Phe chloromethyl ketone (6h, 3 μM) (**D**). $n = 10$ cells per condition from one representative experiment (of three) in (**B-D**). *$P < 0.05$, **$P < 0.01$, ns (not significant) as determined by two-way ANOVA with Tukey's multiple comparison test in (**B-D**).

Figure 7. The LC3B biosensor reports on the CDK1-dependent regulation of the ATG4B-LC3B axis at mitosis (**A**) Representative fluorescence and ΔLifetime images of unsynchronized U2OS cells expressing the WT or G120A biosensor, or cells expressing the WT biosensor and treated with nocodazole-only (16h, 100 ng/ml) or co-treated with nocodazole (16h, 100 ng/ml) and RO-3306 (2h, 2 µM), and analyzed by FRET/FLIM. Squares on the top images of WT or G120A biosensor panels illustrate the location of the enlarged images. Dotted lines on the enlarged images illustrate where the line analysis was performed. Pseudocolor scale: pixel-by-pixel ΔLifetime. Scale bars: overviews, 40 µm; enlarged, 6 µm. Mean ΔLifetime (**B**), number of high ΔLifetime pixels (**C**), line (**D**) and histogram (**E**) analyses of unsynchronized, or nocodazole-only (16h, 100 ng/ml), or nocodazole (16h, 100 ng/ml) and RO-3306 (2h, 2 µM) treated U2OS cells expressing the WT or G120A biosensor in (**B**), (**D**) and (**E**), and the WT donor or biosensor in (**C**). Vertical dotted lines on each histogram depicts the mode value in (**E**). $n = 10$ cells per condition from one representative experiment (of three) in (**B**), (**C**) and (**E**). ****$P < 0.0001$, ns (not significant) as determined by two-way ANOVA with Tukey's multiple comparison test in (**B**) and (**C**).

Figure 1
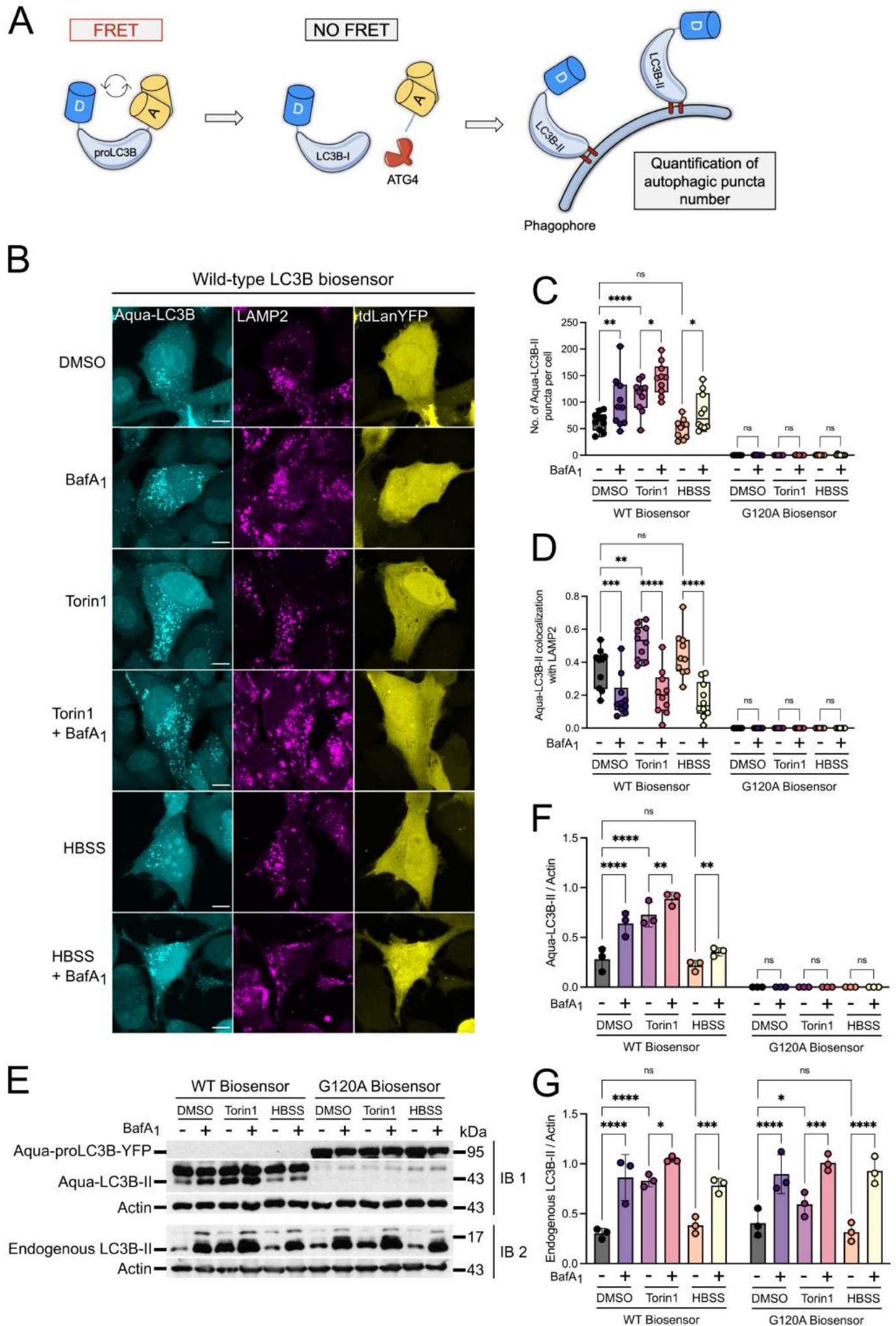
Figure 2
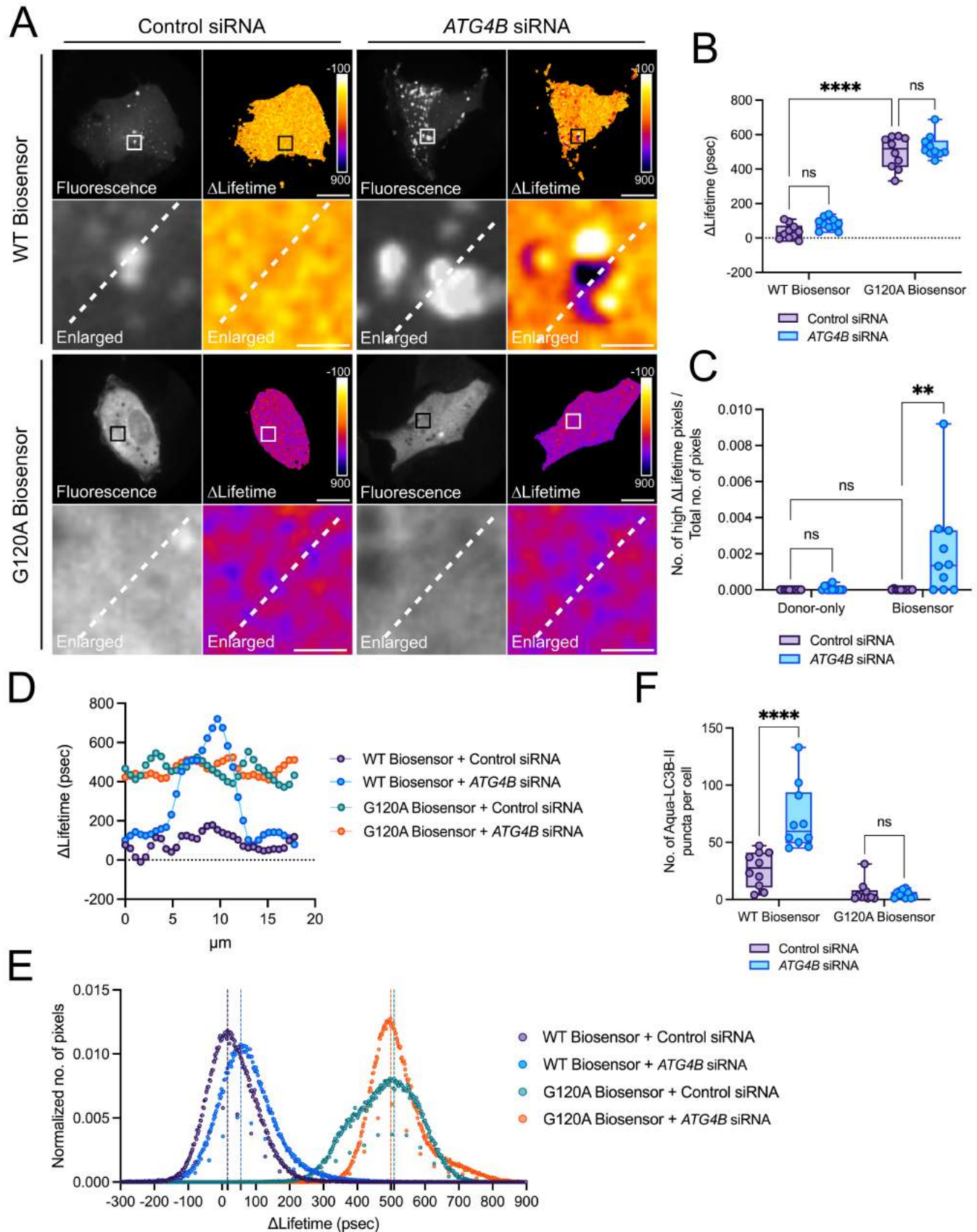
Figure 3
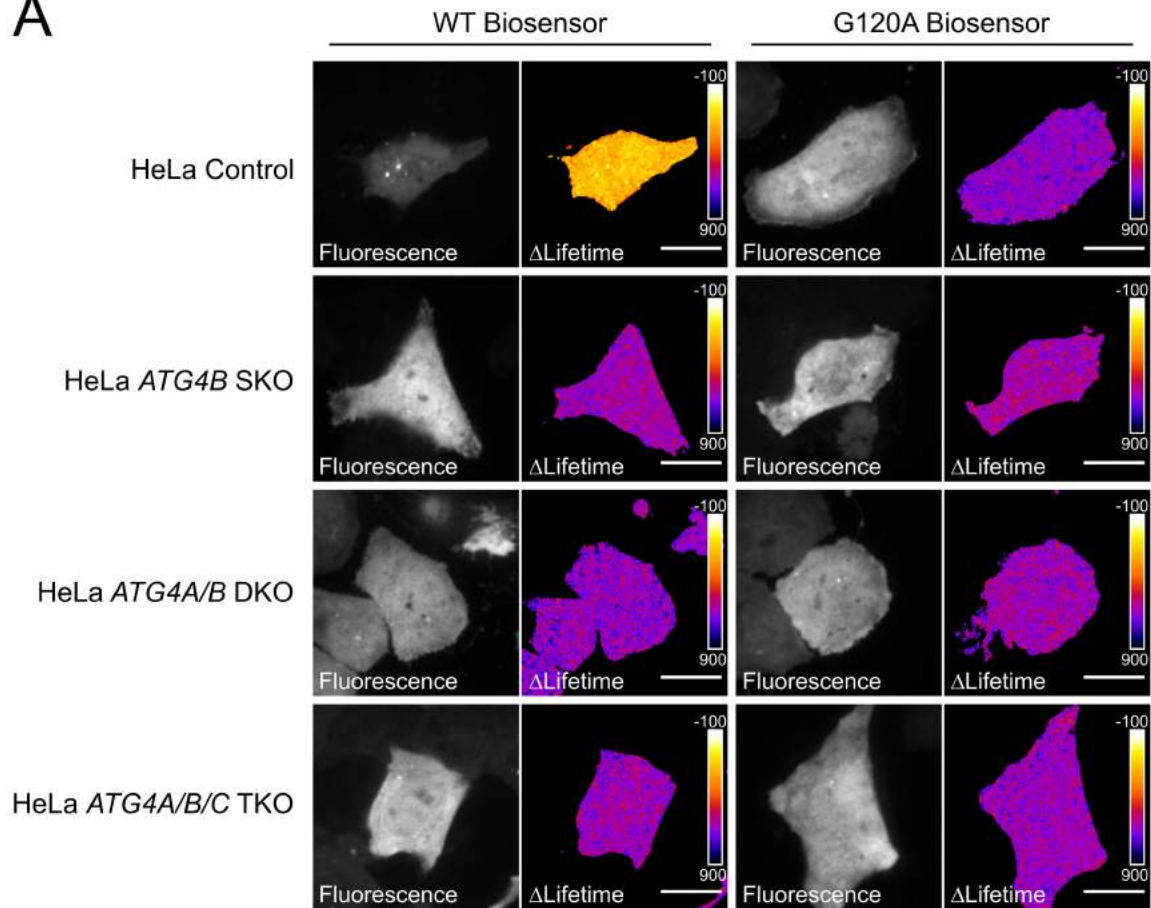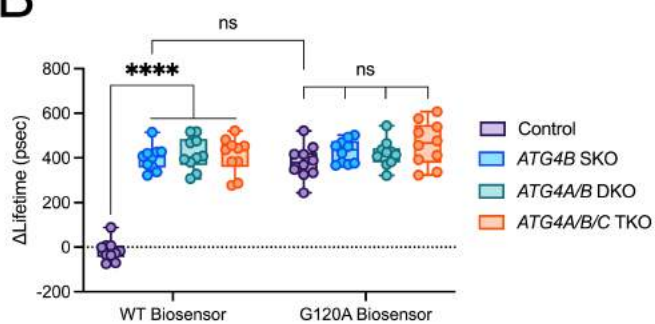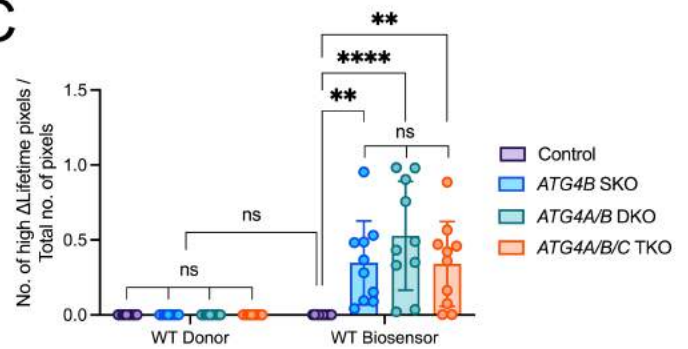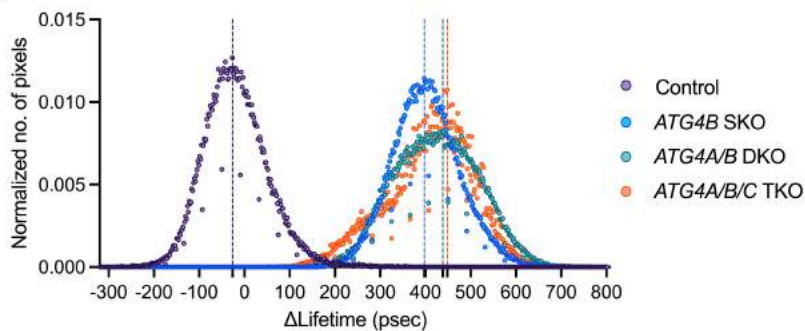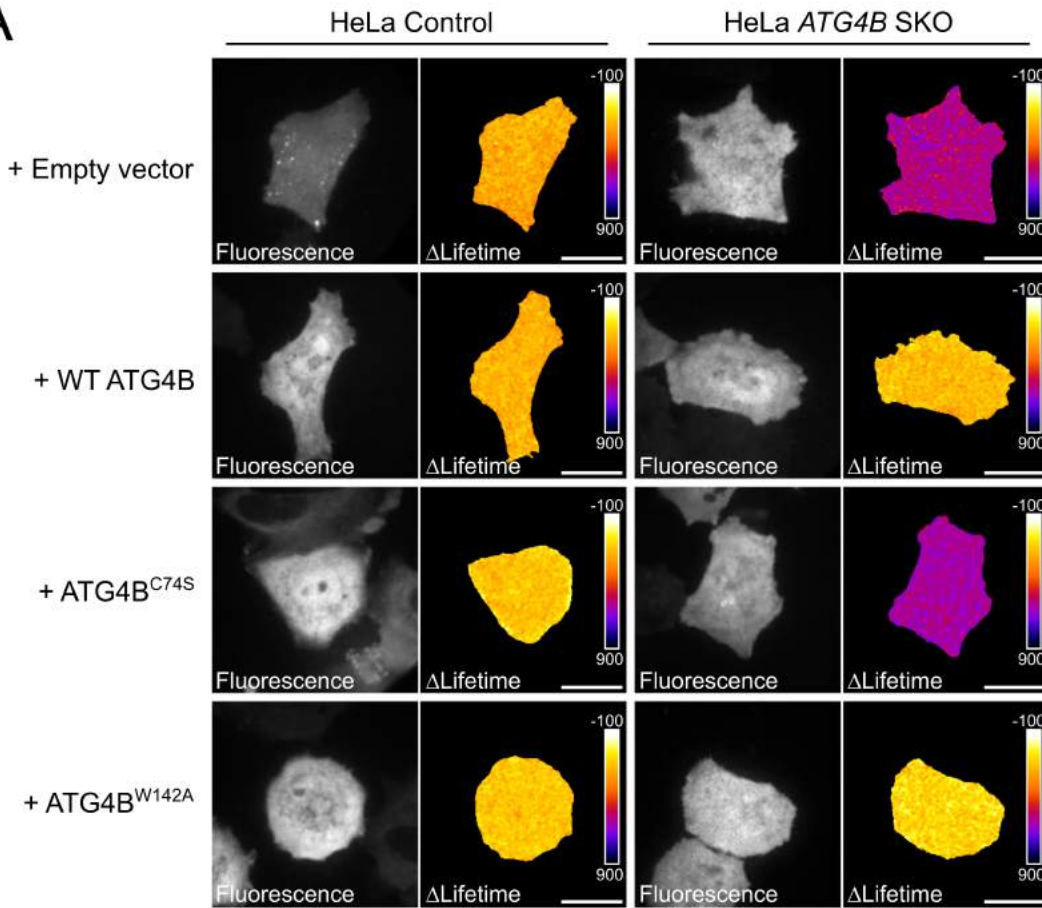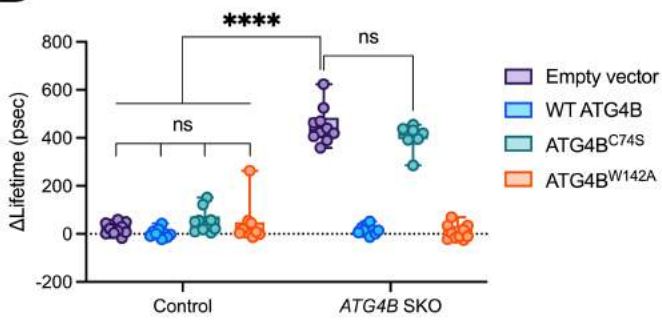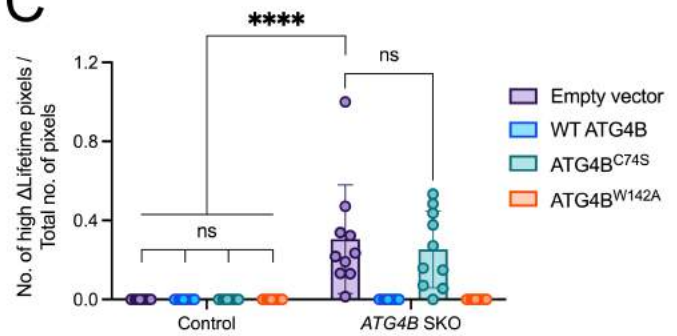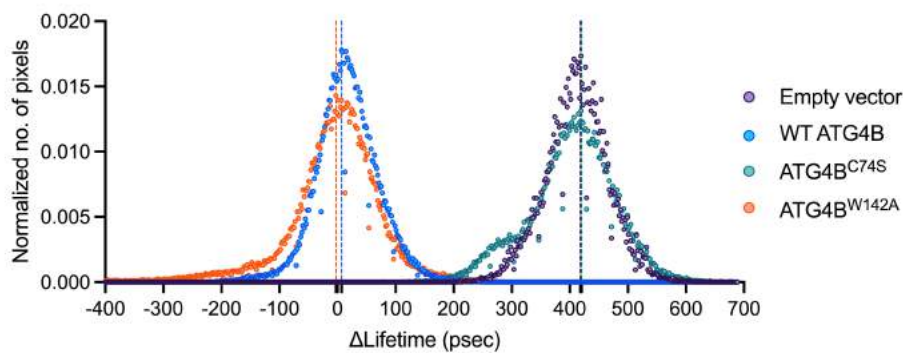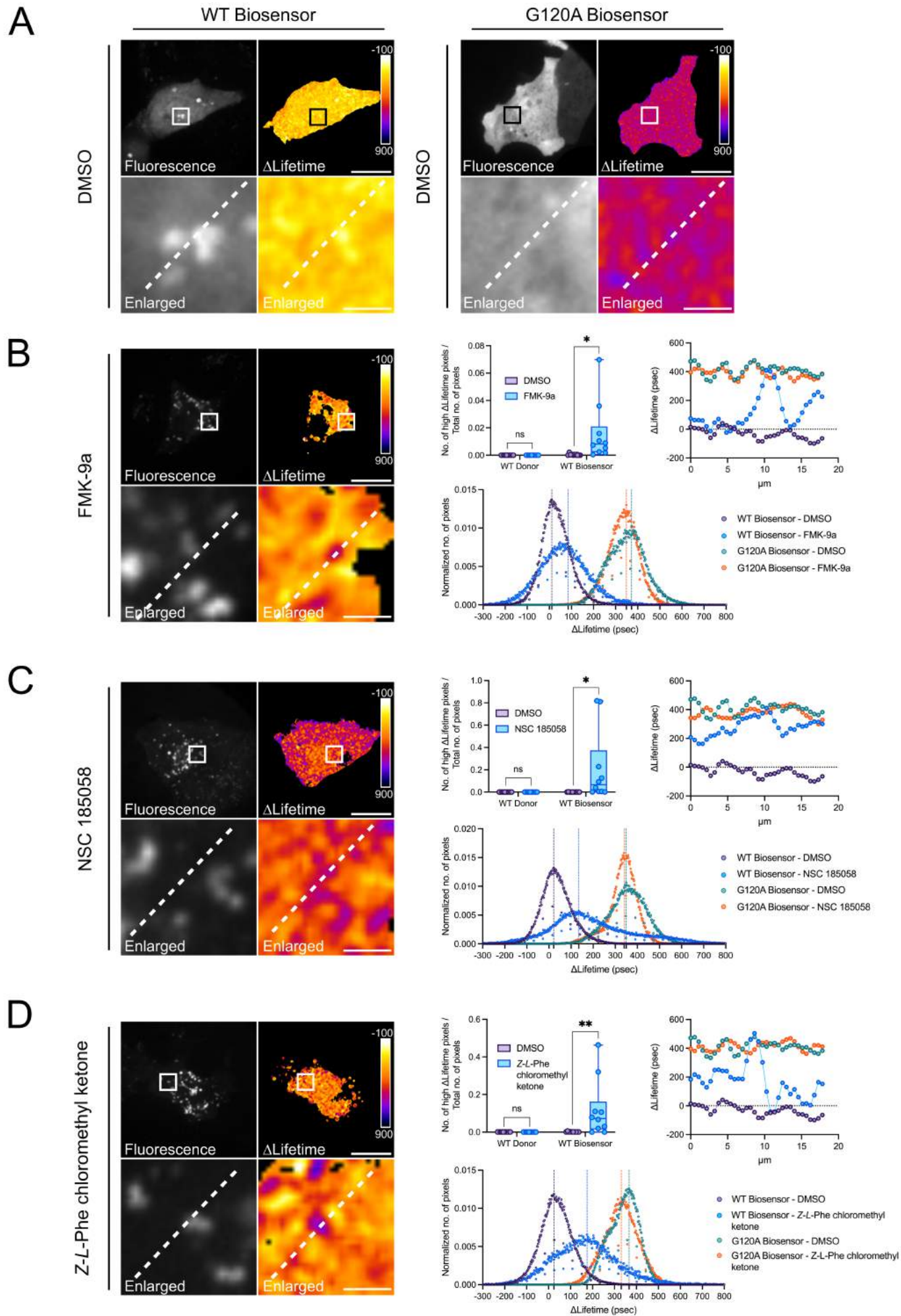
Figure 4

Figure 5

Figure 6

Figure 7